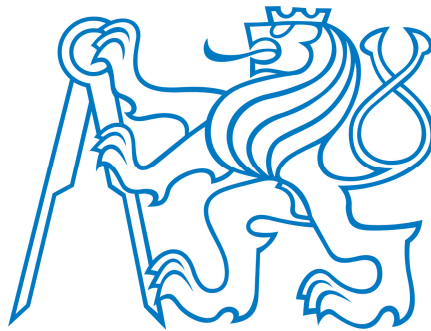


ČESKÉ VYSOKÉ UČENÍ TECHNICKÉ V PRAZE

Fakulta strojní – Ústav technické matematiky



DIPLOMA THESIS

**NUMERICKÉ SIMULACE
ZOBECNĚNÝCH
NEWTONOVSKÝCH TEKUTIN
PRO BIOMEDICÍNSKÉ
APLIKACE**

NUMERICAL SIMULATION OF GENERALISED NEWTONIAN
FLUIDS FOR BIOMEDICAL APPLICATIONS

I declare that I have elaborated this thesis independently and used only the sources listed in the attached bibliography. I have no serious objection to the use of this academic work in accordance with § 60 zákona c. 121/2000 Sb., o právu autorském, o právech souvisejících s právem autorským a o změně některých zákonů (autorský zákon).

Datum:

Podpis

Poděkování

The author would like to express gratitude to his supervisor, doc. Ing. Tomáš Bodnár, Ph.D., for expert guidance throughout the work, provision of necessary study materials, valuable advice, substantive comments, unwavering patience, and willingness.

I. OSOBNÍ A STUDIJNÍ ÚDAJE

Příjmení: **Kalous** Jméno: **Matyáš** Osobní číslo: **484722**
Fakulta/ústav: **Fakulta strojní**
Zadávací katedra/ústav: **Ústav technické matematiky**
Studijní program: **Aplikované vědy ve strojním inženýrství**
Specializace: **Matematické modelování v technice**

II. ÚDAJE K DIPLOMOVÉ PRÁCI

Název diplomové práce:

Numerické simulace zobecněných Newtonovských tekutin pro biomedicínské aplikace

Název diplomové práce anglicky:

Numerical simulations of generalized Newtonian fluids for biomedical applications

Pokyny pro vypracování:

- 1) Popsat zobecněné Newtonovské tekutiny a jejich modely se zaměřením na hemodynamiku.
- 2) Ukázat odvození analytických řešení pro validaci numerických simulací (včetně nestacionárních).
- 3) Užitím vlastního kódu řešit vybrané dvojrozměrné testovací případy.
- 4) Ukázat vliv ne-Newtonovského chování tekutiny (krve) při proudění v kanálech různých tvarů.
- 5) Vyhodnotit získané výsledky vzhledem k použitým rheologickým modelům a numerickým metodám.

Seznam doporučené literatury:

- [1] Feistauer, M., Felcman, J., Straškraba, I.: Mathematical and Computational Methods for Compressible Flow. Clarendon Press, Oxford, 2003, ISBN 0-19-850588-4.
- [2] Galdi, G.P., Rannacher, R., Robertson, A.M., Turek, S., Hemodynamical flows: Modeling, Analysis and Simulation. Birkhauser 2008.
- [3] Fasano, A., Sequeira, A., Hemomath - The Mathematics of Blood. Springer 2017.
- [4] Dvořák, R., Kozel, K.: Matematické modelování v aerodynamice, Vydavatelství ČVUT, 1996.

Jméno a pracoviště vedoucí(ho) diplomové práce:

doc. Ing. Tomáš Bodnár, Ph.D. ústav technické matematiky FS

Jméno a pracoviště druhé(ho) vedoucí(ho) nebo konzultanta(ky) diplomové práce:

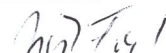
Datum zadání diplomové práce: **18.04.2023**

Termín odevzdání diplomové práce: **13.08.2023**

Platnost zadání diplomové práce: _____



doc. Ing. Tomáš Bodnár, Ph.D.
podpis vedoucí(ho) práce



prof. Ing. Jiří Fůrst, Ph.D.
podpis vedoucí(ho) ústavu/katedry



doc. Ing. Miroslav Španiel, CSc.
podpis děkana(ky)

III. PŘEVZETÍ ZADÁNÍ

Diplomant bere na vědomí, že je povinen vypracovat diplomovou práci samostatně, bez cizí pomoci, s výjimkou poskytnutých konzultací. Seznam použité literatury, jiných pramenů a jmen konzultantů je třeba uvést v diplomové práci.

24.5.2023

Datum převzetí zadání



Podpis studenta

Abstract

Anotace

Diplomová práce se zabývá numerickou simulací zobecněných Newtonovských tekutin se zaměřením na biomedicínské aplikace. Součástí práce je odvození základních rovnic popisujících proudění nestlačitelné tekutiny, definice fyzikálních pojmů, které jsou v práci užívány, a popis analytického řešení Navier-Stokesových rovnic pro zjednodušené případy. K diskretizaci rovnic je užitá metoda konečných objemů umožňující aplikaci na složitější geometrie bez dalších změn a k provázání tlakového pole a pole rychlostí jsou použity metody umělé stlačitelnosti a tlakových korekcí. Tyto dvě metody jsou srovnány na rovném kanále a kanále se stenózou pro nestacionární proudění. Následně je diskutována volba optimální viskozity pro simulace ne-Newtonovského chování pomocí zjednodušeného modelu Newtonovské tekutiny na různých geometriích pro různé tlakové spády.

Klíčová slova: numerická simulace, nestlačitelné proudění, metoda konečných objemů, diskretizace, metoda umělé stlačitelnosti, MacCormackovo schéma, metoda tlakových korekcí, power-law model, optimální viskozita

Abstract

The diploma thesis focuses on the numerical simulation of generalized Newtonian fluids with a focus on biomedical applications. The work includes the derivation of fundamental equations describing the flow of incompressible fluids, definitions of relevant physical concepts used in the study, and the description of analytical solutions to the Navier-Stokes equations for simplified cases. The discretization of equations is achieved through the finite volume method, allowing for application to complex geometries without further modifications. The coupling of pressure and velocity fields is realized using the artificial compressibility and pressure correction methods. These two methods are compared on both a straight channel and a channel with stenosis for unsteady flow scenarios. Subsequently, the selection of optimal viscosity for simulations of non-Newtonian behavior is discussed using a simplified model of Newtonian fluids on various geometries under different pressure gradients.

Keywords: numerical simulation, incompressible flow, finite volume method, discretization, artificial compressibility method, MacCormack scheme, pressure correction method, Power-Law model, optimal viscosity

Contents

1	Introduction	8
1.1	Aim of work	8
1.2	Structure of work	8
2	Physical model	10
2.1	Non-Newtonian fluids	10
2.1.1	Viscosity behavior	10
2.2	Power-law fluids	11
2.3	Properties of blood	12
2.3.1	Viscosity	12
2.3.2	Elasticity	13
2.3.3	Yield Stress	14
2.3.4	Density	14
2.3.5	Thixotropic Behavior	14
3	Mathematical model	15
3.1	Dimensionless numbers	15
3.1.1	Reynolds number	15
3.1.2	Womersley number	16
3.2	Equations of fluid dynamics	16
3.2.1	Description of flow	16
3.2.2	Transport theorem	17
3.2.3	The continuity equation	18
3.2.4	The equations of motion	19
3.2.5	The Navier-Stokes equations	20
3.2.6	Analytical solution for N-S equations	22
3.2.7	Analytical solution for N-S equations for Power-law model fluids	23
3.2.8	Analytical solution for N-S equations under oscillating pressure	25
4	Numerical model	28
4.1	Finite volume method	28
4.2	Finite volumes method discretization	28
4.3	MacCormack scheme	29
4.4	Discretization of inviscid fluxes	29
4.5	Discretization of viscous fluxes	31
4.6	Discretization of pressure derivatives	31
4.7	Artificial compressibility method	32
4.8	Pressure equation	32
4.9	Pressure correction method	33
4.9.1	Solving algorithm for pressure correction method	35
5	Numerical experiments	36
5.1	Used geometries	36
5.2	Validation of artificial compressibility method for oscillating pressure gradient	37
5.2.1	Conclusion	42
5.3	Validation of pressure corrections method for oscillating pressure gradient	42

5.3.1	Conclusion	46
5.4	Simulation driven by oscillating pressure in stenosed channel	46
5.4.1	Results for oscillating pressure in stenosed channel	46
5.4.2	Conclusion	50
5.5	Choosing optimal viscosity	50
5.5.1	Problem setting	50
5.5.2	Simulation in straight channel	51
5.5.3	Results of simulations in straight channel	51
5.5.4	Simulation in stenosed channel	53
5.5.5	Results of simulations in stenosed channel	53
5.5.6	Simulation in curved channel	59
5.5.7	Results on simulations in curved channel	59
5.5.8	Conclusion	64
6	Conclusion	65

1 Introduction

1.1 Aim of work

The primary objective of this work is to present numerical simulations of incompressible non-Newtonian fluids, with a specific focus on their application in the field of biomedicine. We will explore and compare two distinct methods for coupling pressure and velocity within the context of Navier-Stokes equations: the artificial compressibility method and the pressure correction method. Through this comparison, we seek to analyze and compare their respective outcomes in test cases driven by oscillating pressure gradients, mirroring the flow characteristics observed within human veins.

To establish a comprehensive foundation, our approach encompasses two key aspects. Firstly, we undertake a validation exercise by examining the flow between two parallel plates. This validation not only serves to assess the performance of both methods but also allows for a direct comparison against an analytical solution. Subsequently, we extend our investigation to encompass more intricate geometries, thus demonstrating the methods' efficacy in addressing complex flow scenarios.

Another important aspect of this study focuses on understanding the effects of non-Newtonian fluids using the power law model. We aim to gain insights into how these effects can be approximated by choosing the right viscosity parameters in simulations involving Newtonian fluids.

To carry out our investigation, we conducted simulations on three vein-like geometries that resemble those found in the human body. These simulations covered a range of viscosities and explored six different pressure gradients. This approach helps us better grasp how fluid properties interact with varying pressure conditions leading to optimization of viscosity choices in simulations of Newtonian fluids.

To establish the groundwork for our simulations, we will first delve into the characteristics of different non-Newtonian fluids. We will then proceed to derive the Navier-Stokes equations that govern fluid flow. Furthermore, we will showcase the analytical solutions for simplified scenarios such as flow within a tube and between two parallel plates. In addition to these, we will present an analytical solution for the flow of power law fluids and we will provide a solution for fluid flow driven by oscillating pressure, which will serve as a benchmark for comparing the outcomes of our numerical simulations. To solve the Navier-Stokes equations, we will introduce discretization using finite volumes method. This method allows us to transform the continuous governing equations into a discrete form that can be solved numerically and compared to finite difference method, it allows us to use more complex geometries without additional changes. Finally, we will present discretization of said equations using artificial compressibility method and pressure correction method.

1.2 Structure of work

The work is divided into four main logical sections: Physical model, Mathematical model, Numerical model and Numerical experiments.

In Physical model section, we present classification of fluids depending on their behavior of viscosity, we describe power-law fluids and mention key properties of blood.

Mathematical model section primarily familiarizes us with dimensionless numbers such as Reynolds and Womersley number, introduces the fundamental system of equations and essential concepts that will be used in subsequent parts of the work. This

section covers derivation of continuity equation and the Navier-Stokes equations for incompressible fluids and shows analytical solutions for simplified cases of flow in a tube and between two parallel plates for Newtonian fluid driven by constant pressure, for power-law model of fluid driven by constant pressure and for Newtonian fluid driven by oscillating pressure.

The third section, Numerical model, seeks to explain discretization using finite volumes method and shows us two ways of coupling pressure and velocity for incompressible fluids, artificial compressibility method and pressure correction method.

In last section, Numerical experiments, we present two sets of experiments conducted using solver in MATLAB. First set aims to show simulations driven by oscillating pressure and their solution using artificial compressibility method and pressure correction method and comparison of their results on straight channel, where we are able to compare results with analytical solution, and on stenosed channel, to show advantage of finite volumes method to be easily used on complex geometries. Second set of experiments aims to compare Newtonian and non-Newtonian fluids for steady cases and to show optimal viscosity to describe non-Newtonian model as Newtonian. We present three different cases: simulation on straight channel, simulation on stenosed channel and simulation on curved channel. To compare the results, we present Euclidian norm of difference between velocity fields of Newtonian and non-Newtonian fluid.

2 Physical model

The "Physical model" section of our study delves into the foundational aspects of the physical properties that define the behavior of non-Newtonian fluids, particularly focusing on the characteristics of power-law fluids and their relevance to the dynamics of blood. By understanding the fundamental properties of these fluids, we can gain valuable insights into their intricate behavior and its implications for various applications.

In this section, we embark on a comprehensive exploration of non-Newtonian fluids, a class of substances that deviate from the classic linear relationship between shear stress and shear rate. We begin by delving into the concept of viscosity behavior, which plays a pivotal role in describing how these fluids respond to external forces. Understanding the nature of non-Newtonian fluids is crucial for accurate modeling and prediction of their behavior in real-world scenarios.

2.1 Non-Newtonian fluids

Non-Newtonian fluids encompass a wide range of fluids that exhibit complex flow behavior and do not adhere to the linear relationship between shear stress and shear rate observed in Newtonian fluids. Understanding the behavior of non-Newtonian fluids requires classifying them based on their unique rheological characteristics. Various classification schemes have been proposed to categorize non-Newtonian fluids, taking into account different aspects of their flow behavior.

2.1.1 Viscosity behavior

Viscosity behavior is an essential characteristic that helps classify non-Newtonian fluids into distinct categories. The classification scheme for non-Newtonian fluids is based on their response to different levels of shear stress and time-dependent deformation. This classification plays a fundamental role in understanding and characterizing the complex rheological properties of these fluids. Moreover, it enables engineers and researchers to design and optimize processes involving non-Newtonian fluids in various industries, including polymer processing, food production, pharmaceuticals, and biotechnology.

Newtonian fluids Newtonian fluids represent a fundamental class of fluids that exhibit a linear relationship between the applied shear stress and the resulting rate of deformation. This characteristic behavior is encapsulated by Newton's law of viscosity, which states that the shear stress is directly proportional to the velocity gradient. In simpler terms, the viscosity of a Newtonian fluid remains constant regardless of the magnitude of the applied shear force. This distinctive property of Newtonian fluids makes them particularly amenable to analysis and prediction using classical fluid dynamics principles. Their predictable and linear response to shear forces simplifies the mathematical modeling and simulation of fluid flow in a wide range of scenarios. Despite their simplicity, Newtonian fluids are a crucial reference point for understanding the more complex rheological behaviors observed in non-Newtonian

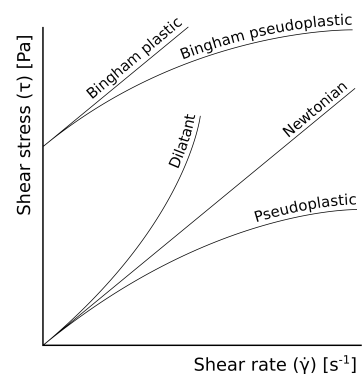


Figure 1: Classification of fluids with shear stress as a function of shear rate [29]

fluids. Water and most common gases, like air, are prime examples of Newtonian fluids.

Shear-thinning (pseudoplastic) fluids Moving beyond Newtonian fluids, the second class encompasses shear-thinning (pseudoplastic) fluids. In this category, the viscosity decreases as the shear rate increases. These fluids are also known as pseudoplastic fluids. Shear-thinning behavior is common in solutions containing long-chain polymers or colloidal particles, where the macromolecules tend to align and slide past each other under shear. The result is a reduced apparent viscosity at higher shear rates, allowing for easier flow. This behavior is of significant interest in the formulation of paints, cosmetics, and various industrial processes.

Shear-thickening (dilatant) fluids A contrasting behavior can be observed in the third class, known as shear-thickening (dilatant) fluids. Here, the viscosity increases as the shear rate rises. These fluids are also called dilatant fluids. Unlike shear-thinning fluids, shear-thickening fluids exhibit resistance to flow under low shear rates and suddenly become less viscous under high shear rates. An interesting example is a mixture of cornstarch and water, known as "oobleck." Under low shear conditions, it behaves like a fluid, but when subjected to high shear forces, it transforms into a solid-like state.

Bingham plastic fluids The fourth class comprises Bingham plastic fluids. Bingham plastics behave like rigid solids until a certain yield stress is exceeded. Once the yield stress is surpassed, they flow as viscous liquids. Toothpaste and some mud-like substances display Bingham plastic behavior. This behavior is particularly relevant in engineering applications where materials need to be in a stable state when not in motion but transition smoothly into a flowing state when subjected to sufficient force.

Thixotropic fluids Additionally, there are thixotropic fluids, which become less viscous over time when subjected to constant shear stress. Once the shear stress is removed, they recover their original viscosity. Thixotropic behavior is commonly observed in certain paints, gels, and drilling fluids. It plays a crucial role in industrial applications that require time-dependent changes in viscosity, such as inkjet printing and adhesives [1].

Rheopectic fluids Another intriguing category is rheopectic fluids, which demonstrate the opposite behavior to thixotropic fluids. Rheopectic fluids show an increase in viscosity with time under constant shear stress. However, upon stress removal, they exhibit a decrease in viscosity. Certain colloidal suspensions and printing inks demonstrate rheopectic properties. Rheopectic fluids are employed in applications where gradual changes in viscosity are necessary to optimize processes and material performance. [2], [14]

2.2 Power-law fluids

Power-law fluids, also known as Ostwald-de Waele fluids, are a class of generalized Newtonian fluids that exhibit a non-linear relationship between shear stress and shear

rate. They are characterized by the Power-law model, which describes this relationship as a power-law equation:

$$\tau = K \cdot \left| \frac{\partial u}{\partial y} \right|^\kappa = K \cdot \dot{\gamma}^\kappa \quad (1)$$

where τ is the shear stress, $\dot{\gamma}$ is the shear rate, K is the flow consistency index, and κ is the flow behavior index.

Apparent or effective viscosity μ_{eff} is then obtained as

$$\mu_{eff} = K \cdot \left| \frac{\partial u}{\partial y} \right|^{\kappa-1} = K \cdot \dot{\gamma}^{\kappa-1} \quad (2)$$

The flow consistency index K represents the fluid's resistance to flow and determines the magnitude of the shear stress for a given shear rate. A higher value of K indicates a more viscous fluid, while a lower value indicates a less viscous fluid.

The flow behavior index κ characterizes the non-Newtonian behavior of the fluid. For $\kappa < 1$, the fluid exhibits shear-thinning behavior, where the apparent viscosity decreases as the shear rate increases. This behavior is commonly observed in many fluids, including polymer solutions and suspensions. On the other hand, for $\kappa > 1$, the fluid exhibits shear-thickening behavior, where the apparent viscosity increases with increasing shear rate. Shear-thickening behavior is less common but can be observed in certain complex fluids.

The Power-law model provides a simple yet effective means of describing the flow behavior of Power-law fluids over a wide range of shear rates. It is widely used in various industries and applications, including polymer processing, food processing, oil and gas, and biomedical engineering.

It is important to note that the Power-law model is an empirical model that does not capture all the complexities of real fluids. In some cases, more advanced rheological models, such as the Powell-Eyring model or the Carreau-Yasuda model, may be required to accurately describe the flow behavior of certain fluids. These models and constants for simulation of blood behavior can be seen in Tab. 1.

When working with Power-law fluids, it is crucial to determine the appropriate values of the flow consistency index K and the flow behavior index κ based on experimental measurements or empirical correlations specific to the fluid of interest. These parameters play a crucial role in accurately predicting the flow characteristics and designing processes involving Power-law fluids.

2.3 Properties of blood

Blood is a complex non-Newtonian fluid that plays a crucial role in the human body's circulatory system. It exhibits unique rheological properties that are essential for its physiological functions. Understanding the properties of blood is of great significance in medical and biological research. Here are some key properties of blood:

2.3.1 Viscosity

Blood exhibits a shear-thinning behavior, meaning its viscosity decreases with increasing shear rate. This property is attributed to the presence of red blood cells, plasma proteins, and other components in the blood. At low shear rates, the impact of blood

Model Name	Model Equation	Model Coefficients
Modified Cross	$\mu = \mu_\infty + (\mu_0 - \mu_\infty) \left[\frac{1}{[1+(\lambda\dot{\gamma})^K]^\alpha} \right]$	$\mu_0 = 0.056 \text{ Pa}\cdot\text{s}$, $\mu_\infty = 0.00345 \text{ Pa}\cdot\text{s}$, $\lambda = 3.736 \text{ s}$, $K = 2.406$, $\alpha = 0.254$
Powell-Eyring	$\mu = \mu_\infty + (\mu_0 - \mu_\infty) \left[\frac{\sinh^{-1} \alpha \dot{\gamma}}{\lambda \dot{\gamma}} \right]$	$\mu_0 = 0.056 \text{ Pa}\cdot\text{s}$, $\mu_\infty = 0.00345 \text{ Pa}\cdot\text{s}$, $\lambda = 5.383 \text{ s}$
Modified Powell-Eyring	$\mu = \mu_\infty + (\mu_0 - \mu_\infty) \left[\frac{\ln(\lambda\dot{\gamma}+1)}{[\lambda\dot{\gamma}]^K} \right]$	$\mu_0 = 0.056 \text{ Pa}\cdot\text{s}$, $\mu_\infty = 0.00345 \text{ Pa}\cdot\text{s}$, $\lambda = 2.415 \text{ s}$, $K = 1.089$
Cross	$\mu = \mu_\infty + (\mu_0 - \mu_\infty) \left[\frac{1}{[1+\lambda\dot{\gamma}]^K} \right]$	$\mu_0 = 0.056 \text{ Pa}\cdot\text{s}$, $\mu_\infty = 0.00345 \text{ Pa}\cdot\text{s}$, $\lambda = 1.007 \text{ s}$, $K = 1.028$
Simplified Cross	$\mu = \mu_\infty + (\mu_0 - \mu_\infty) \left[\frac{1}{1+\lambda\dot{\gamma}} \right]$	$\mu_0 = 0.13 \text{ Pa}\cdot\text{s}$, $\mu_\infty = 0.005 \text{ Pa}\cdot\text{s}$, $\lambda = 8.0 \text{ s}$
Carreau	$\mu = \mu_\infty + (\mu_0 - \mu_\infty) [1 + (\lambda\dot{\gamma})^2]^{\frac{\kappa-1}{2}}$	$\mu_0 = 0.056 \text{ Pa}\cdot\text{s}$, $\mu_\infty = 0.00345 \text{ Pa}\cdot\text{s}$, $\lambda = 3.313 \text{ s}$, $\kappa = 0.3568$
Carreau-Yasuda	$\mu = \mu_\infty + (\mu_0 - \mu_\infty) [1 + (\lambda\dot{\gamma})^\alpha]^{\frac{\kappa-1}{\alpha}}$	$\mu_0 = 0.056 \text{ Pa}\cdot\text{s}$, $\mu_\infty = 0.00345 \text{ Pa}\cdot\text{s}$, $\lambda = 1.902 \text{ s}$, $\kappa = 0.22$, $\alpha = 1.25$
Power-Law	$\mu = K\dot{\gamma}^{\kappa-1}$	$\mu_{\min} = 0.00345 \text{ Pa}\cdot\text{s}$, $\mu_{\max} = 0.056 \text{ Pa}\cdot\text{s}$, $\kappa = 0.60$, $K = 0.35$

Table 1: More advanced models and their parameters for simulation of blood according to [5]

hematocrit on viscosity is higher, while at high shear rates, it flows more easily due to the alignment and deformation of red blood cells. The viscosity of blood is typically measured in centipoise [cP] or millipascal-seconds [mPa·s] and can range from 3 to 4.5 cP (0.003 to 0.0045 Pa·s) for whole blood [3].

2.3.2 Elasticity

Blood shows viscoelastic behavior, which means it possesses both viscous and elastic properties. This property allows blood to deform under stress and recover its original shape when the stress is removed. The elasticity of blood is primarily due to the presence of red blood cells, which can undergo reversible changes in shape and deformability. The elastic modulus of blood, a measure of its elasticity, can vary depending on factors such as hematocrit and shear rate, but typical values range from 1 to 5 Pascal. [24].

2.3.3 Yield Stress

Blood exhibits a yield stress, which is the minimum stress required to initiate flow. Below the yield stress, blood behaves as a solid-like material and resists deformation. The yield stress of blood is crucial in maintaining the integrity of blood vessels and preventing excessive bleeding. The yield stress of blood is estimated to be in the range of 0.05 to 0.3 Pascal [Pa], depending on factors such as hematocrit and temperature [24].

2.3.4 Density

The density of blood refers to its mass per unit volume. The average density of blood is around 1060 kilograms per cubic meter [kg/m^3] or 1.06 grams per cubic centimeter [g/cm^3] [17]. The density of blood may vary slightly depending on factors such as hematocrit and the presence of dissolved substances.

2.3.5 Thixotropic Behavior

Blood also displays thixotropic behavior, where its viscosity decreases over time under constant shear stress. This property is related to the reversible breakdown of blood clots or aggregates under continuous shear, allowing blood to flow more freely. Once the shear stress is removed, the viscosity of blood recovers, preventing excessive bleeding [27].

3 Mathematical model

The "Mathematical Model" section serves as the cornerstone of our study, providing a vital framework for analyzing fluid dynamics in the context of non-Newtonian behavior. It encompasses essential concepts and equations that underpin our investigation.

We begin by introducing dimensionless numbers, particularly the Reynolds number, which offers insights into the relative importance of inertial and viscous forces. This fundamental concept provides a universal basis for fluid behavior analysis.

Moving forward, we delve into the equations of fluid dynamics, starting with the description of flow and the transport theorem. These concepts provide tools to understand how fluids interact and how properties are transported within them.

The continuity equation is then explored, shedding light on mass conservation within fluid systems. This equation is pivotal in grasping the fundamental principles governing fluid motion.

The core of fluid dynamics—the Navier-Stokes equations—takes center stage, elucidating the intricate relationship between pressure, velocity, and viscous forces. These equations offer a comprehensive view of fluid behavior.

Furthermore, we investigate analytical solutions for the Navier-Stokes equations, providing insights into fluid dynamics under various conditions. This includes scenarios involving power-law model fluids and oscillating pressure.

Together, these sections establish a robust mathematical foundation for our subsequent analyses and simulations. The integration of dimensionless numbers, governing equations, and analytical solutions empowers us to comprehensively explore non-Newtonian fluid dynamics, yielding valuable insights into their behavior across different contexts.

3.1 Dimensionless numbers

3.1.1 Reynolds number

The Reynolds number (Re) is a dimensionless parameter that characterizes the flow regime of a fluid within a given system. It quantifies the relative importance of inertial forces to viscous forces and provides insights into the dominant mechanisms at play. The Reynolds number is calculated by dividing the product of the characteristic length scale (L), the flow velocity (U), and the fluid density (ρ) by the dynamic viscosity (μ):

$$Re = \frac{\rho \cdot U \cdot L}{\mu}$$

where ρ represents the fluid density, U is the characteristic flow velocity, L denotes the characteristic length scale, and μ is the dynamic viscosity of the fluid.

The Reynolds number serves as a key parameter for characterizing the flow behavior. At low Reynolds numbers, the flow is typically laminar, characterized by smooth and predictable motion. As the Reynolds number increases, the flow becomes more turbulent, exhibiting chaotic and random motion. The transition from laminar to turbulent flow depends on various factors, including fluid properties, geometry, and flow conditions.

In the field of fluid dynamics, the Reynolds number has significant implications. It aids in the classification of flow regimes and guides the selection of appropriate mathematical models. [23], [28]

3.1.2 Womersley number

The Womersley number Wo is a dimensionless parameter that characterizes the pulsatile flow behavior in fluid dynamics. It is defined as the product of the pulsatile flow frequency ω and the characteristic length scale L , divided by the dynamic viscosity μ . Mathematically, it can be expressed as:

$$Wo = \frac{H}{2} \sqrt{\frac{\omega \cdot \rho}{\mu}}$$

where ω represents the pulsatile frequency, H is the characteristic length scale of the system, μ denotes the dynamic viscosity of the fluid, and ρ is the density of the fluid.

The Womersley number provides valuable information about the relative importance of inertial effects to viscous effects in pulsatile flow. A low Womersley number indicates that the flow is dominated by viscous effects, while a high Womersley number suggests a significant influence of inertial forces.

When the Womersley number $Wo < 1$, the fluid behaves in a "quasi-steady" manner, meaning that the instantaneous flow rate is determined by the instantaneous pressure gradient. In this regime, the fluid responds relatively quickly to changes in pressure. However, it is essential to note that "quasi-steady" does not imply that the flow is not changing over time. Instead, it refers to the fluid's ability to keep up with rapidly changing pressure gradients, even if the flow exhibits significant oscillations.

On the other hand, when the Womersley number $Wo > 1$, the fluid's behavior deviates more and more from quasi-steady behavior. In this regime, the fluid responds less promptly to changes in pressure, and its flow behavior becomes more influenced by inertial effects. [18], [30]

Table 2: Fluid Flow Parameters in Various Blood Vessels [19]

Blood Circulatory System	Wo	Average Velocity v [m/s]	Re
Systemic Circulation			
Ascending Aorta	21	0.18	1500
Abdominal Aorta	12	0.14	640
Renal Artery	4	0.40	700
Femoral Artery	4	0.12	2200
Femoral Vein	7	0.04	104
Superior Vena Cava	15	0.09	550
Inferior Vena Cava	17	0.21	1400
Pulmonary Circulation			
Pulmonary Artery	20	0.19	1600
Pulmonary Vein	10	0.19	800

3.2 Equations of fluid dynamics

3.2.1 Description of flow

We describe fluid motion in two ways:

The Lagrangian approach We describe trajectories of each individual particles by the equation

$$x = \varphi(X, t) \quad (3)$$

Or in detailed notation

$$x = \varphi(X, t_0, t), \quad (4)$$

which describes position x at the time t of the particle passing through the point X at time t_0 .

We can obtain velocity and acceleration of the fluid particle as derivatives of relations (3) and (4) (given the derivatives exist) respectively

$$\begin{aligned} \hat{\mathbf{v}}(X, t) &= \frac{\partial \varphi}{\partial t}(X, t) \\ \hat{\mathbf{a}}(X, t) &= \frac{\partial^2 \varphi}{\partial t^2}(X, t) \end{aligned} \quad (5)$$

[9]

The Eulerian approach We describe the flow of fluid by determining the velocity $\mathbf{v}(x, t)$ of fluid particle passing through the point x at time t . Using (3) and (5), we can write

$$\mathbf{v}(x, t) = \hat{\mathbf{v}}(X, t) = \frac{\partial \varphi}{\partial t}(X, t) \quad (6)$$

where $x = \varphi(X, t)$. The acceleration is then expressed as

$$\begin{aligned} \mathbf{a}(x, t) &= \frac{\partial \mathbf{v}}{\partial t}(x, t) + (\mathbf{v}(x, t) \cdot \text{grad}) \mathbf{v}(x, t) \\ &= \frac{\partial \mathbf{v}}{\partial t}(x, t) + (\mathbf{v}(x, t) \cdot \nabla) \mathbf{v}(x, t) \end{aligned} \quad (7)$$

If we define material derivative with respect to time

$$\frac{D}{Dt} = \frac{\partial}{\partial t} + \mathbf{v} \cdot \text{grad} = \frac{\partial}{\partial t} + \mathbf{v} \cdot \nabla \quad (8)$$

we can rewrite acceleration as

$$\mathbf{a} = \frac{D\mathbf{v}}{Dt} := \frac{\partial \mathbf{v}}{\partial t} + (\mathbf{v} \cdot \text{grad}) \mathbf{v} \quad (9)$$

[9]

3.2.2 Transport theorem

Let a function $F = F(x, t) : \mathcal{M} \rightarrow \mathbb{R}$ be representation of physical quantity transported by fluid particles and described by Eulerian approach, we consider a system of fluid particles filling a bounded domain $\mathcal{V}(t) \subset \Omega_t$ at time t . We can obtain the total amount of the quantity in the volume $\mathcal{V}(t)$ at time t given by the function F by the integral

$$\mathcal{F}(t) = \int_{\mathcal{V}(t)} F(x, t) dx \quad (10)$$

We are interested in the rate of change of the quantity F , in derivative in other words

$$\frac{d\mathcal{F}(t)}{dt} = \frac{d}{dt} \int_{\mathcal{V}(t)} F(x, t) dx \quad (11)$$

Let the function $F = F(x, t)$ have continuous and bounded first order derivatives on set $\{(x, t); t \in (t_1, t_2), x \in \mathcal{V}(t)\}$, then for each $t \in (t_1, t_2)$, there exists a finite derivative

$$\begin{aligned} \frac{d\mathcal{F}}{dt}(t) &= \frac{d}{dt} \int_{\mathcal{V}(t)} F(x, t) dx \\ &= \int_{\mathcal{V}(t)} \left[\frac{\partial F}{\partial t}(x, t) + \mathbf{v}(x, t) \cdot \text{grad} F(x, t) + F(x, t) \text{div} \mathbf{v}(x, t) \right] dx \\ &= \int_{\mathcal{V}(t)} \left[\frac{\partial F}{\partial t}(x, t) + \text{div}(F\mathbf{v})(x, t) \right] dx \end{aligned} \quad (12)$$

For further and more detailed explanation, see [9], [8] or [6].

3.2.3 The continuity equation

Mass $m(\mathcal{V}; t)$ of the fluid contained in any subdomain $\mathcal{V}(t) \subset \Omega_t$ can be determined by integral

$$m(\mathcal{V}; t) = \int_{\mathcal{V}} \rho(x, t) dx, \quad (13)$$

where ρ is function of fluid density

$$\rho : \mathcal{M} = \{(x, t); t \in (0, T), x \in \Omega_t\} \rightarrow (0, +\infty) \quad (14)$$

The domain $\mathcal{V}(t)$ contains same particles at each time instant, that filled a bounded domain called a control volume $\mathcal{V}(t_0)$ at the time $t_0 \in (0, T)$, therefore the mass of piece of fluid represented by domain $\mathcal{V}(t)$ does not depend on time t .

This can be expressed by the equation

$$\frac{dm(\mathcal{V}(t); t)}{dt} = 0, \quad t \in (t_1, t_2) \quad (15)$$

where $t \in (t_1, t_2)$ is sufficiently small time interval.

Using transport theorem and $F = \rho$, we get the identity

$$\int_{\mathcal{V}(t)} \left[\frac{\partial \rho}{\partial t}(x, t) + \text{div}(\rho\mathbf{v})(x, t) \right] dx = 0, \quad t \in (t_1, t_2) \quad (16)$$

We can now substitute $t := t_0$ and $\mathcal{V}(t_0) = \mathcal{V}$ and for an arbitrary $t_0 \in (0, T)$ and an arbitrary control volume \mathcal{V} in Ω_{t_0} we obtain

$$\int_{\mathcal{V}} \left[\frac{\partial \rho}{\partial t}(x, t_0) + \text{div}(\rho\mathbf{v})(x, t_0) \right] dx = 0 \quad (17)$$

Expecting continuity of the integrand 17 and relabeling t_0 as t , we get the differential form of the law of conservation of mass also called the continuity equation:

$$\frac{\partial \rho}{\partial t} (x, t) + \operatorname{div} (\rho (x, t) \mathbf{v} (x, t)) = 0, \quad t \in (0, T), x \in \Omega_t. \quad (18)$$

[9]

3.2.4 The equations of motion

The total momentum of particles contained in $\mathcal{V} (t)$ is given by

$$\mathcal{H} (\mathcal{V} (t)) = \int_{\mathcal{V} (t)} \rho (x, t) \mathbf{v} (x, t) dx. \quad (19)$$

Denoting by $\mathcal{F} (\mathcal{V} (t))$ the force acting on volume $\mathcal{V} (t)$, the law of conservation of momentum states the rate of change of the total momentum of a piece of fluid formed by the same particles at each time, is equal to the said force:

$$\frac{d\mathcal{H} (\mathcal{V} (t))}{dt} = \mathcal{F} (\mathcal{V} (t)), \quad t \in (t_1, t_2) \quad (20)$$

Using transport theorem we get

$$\int_{\mathcal{V} (t)} \left[\frac{\partial}{\partial t} (\rho (x, t) v_i (x, t)) + \operatorname{div} (\rho (x, t) v_i (x, t) \mathbf{v} (x, t)) \right] dx = \mathcal{F}_i (\mathcal{V} (t)), \quad (21)$$

$$i = 1, 2, 3, t \in (t_1, t_2)$$

By taking into account arbitrary time instant t and arbitrary control volume \mathcal{V} we can rewrite 21 as

$$\int_{\mathcal{V}} \left[\frac{\partial}{\partial t} (\rho (x, t) v_i (x, t)) + \operatorname{div} (\rho (x, t) v_i (x, t) \mathbf{v} (x, t)) \right] dx = \mathcal{F}_i (\mathcal{V}; t), \quad (22)$$

$$i = 1, 2, 3, \text{ for arbitrary } t$$

We distinguish two types of force $\mathcal{F} (\mathcal{V}; t)$ acting in fluids:

The volume force also called outer or body force expressed by its density \mathbf{f} :

$$\mathcal{F}_v (\mathcal{V}; t) = \int_{\mathcal{V}} \rho (x, t) \mathbf{f} (x, t) dx. \quad (23)$$

The surface force or inner force, by which the fluid outside of \mathcal{V} acts on a set $S \subset \partial \mathcal{V}$, expressed by stress vector $\mathbf{T} (x, t, \mathbf{n})$.

$$\mathbf{F}_S = \int_S \mathbf{T} (x, t, \mathbf{n} (x)) dS. \quad (24)$$

To express the stress vector, we choose normals parallel to the coordinate axes and set

$$\tau_{ij} = T_i (x, t, e_j), \quad i, j = 1, 2, 3, \quad (25)$$

$$e_1 = (1, 0, 0), \quad e_2 = (0, 1, 0), \quad e_3 = (0, 0, 1)$$

Then

$$T_i(x, t, \mathbf{n}) = \sum_{j=1}^3 n_j \tau_{ij}(x, t), \quad i = 1, 2, 3. \quad (26)$$

For general fluid we obtain equation

$$\begin{aligned} & \int_{\mathcal{V}} \left[\frac{\partial}{\partial t} (\rho(x, t) v_i(x, t)) + \operatorname{div} (\rho(x, t) v_i(x, t) \mathbf{v}(x, t)) \right] dx \\ &= \int_{\mathcal{V}} \rho(x, t) \mathbf{f}(x, t) dx + \int_{\partial \mathcal{V}} \sum_{j=1}^3 \tau_{ij}(x, t) n_j(x) dS, \quad i = 1, 2, 3, \end{aligned} \quad (27)$$

for each $t \in (0, T)$ and arbitrary control volume \mathcal{V} in Ω_t .

By applying Green's theorem, we can rewrite equation 27 as

$$\frac{\partial}{\partial t} (\rho v_i) + \operatorname{div} (\rho v_i \mathbf{v}) = \rho f_i + \sum_{j=1}^3 \frac{\partial \tau_{ij}}{\partial x_j}, \quad i = 1, 2, 3, \quad (28)$$

or

$$\frac{\partial}{\partial t} (\rho \mathbf{v}) + \operatorname{div} (\rho \mathbf{v} \otimes \mathbf{v}) = \rho \mathbf{f} + \operatorname{div} \mathcal{T} \quad (29)$$

[9]

3.2.5 The Navier-Stokes equations

Under conditions further described in [10], the stress tensor can be expressed as \mathcal{T}

$$\mathcal{T} = (-p + \lambda \operatorname{div} \mathbf{v}) \mathbb{I} + 2\mu \mathbb{D}(\mathbf{v}), \quad (30)$$

where μ, λ are first and second viscosity coefficients, respectively, \mathbb{I} is unit tensor and \mathbb{D} is deformation velocity tensor:

$$\mathbb{D} = \mathbb{D}(\mathbf{v}) = (d_{i,j})_{i,j=1}^3, \quad d_{i,j} = \frac{1}{2} \left(\frac{\partial v_i}{\partial x_j} + \frac{\partial v_j}{\partial x_i} \right). \quad (31)$$

We can substitute relation (30) into the general equations of motion (29) and get so-called Navier-Stokes equations

$$\frac{\partial}{\partial t} (\rho \mathbf{v}) + \operatorname{div} (\rho \mathbf{v} \otimes \mathbf{v}) = \rho \mathbf{f} - \operatorname{grad} p + \operatorname{grad} (\lambda \operatorname{div} \mathbf{v}) + \operatorname{div} (2\mu \mathbb{D}(\mathbf{v})) \quad (32)$$

Provided the continuity equation (18) is satisfied and considering incompressible viscous fluid with constant density in three dimensional case, we can express (32) and (18) as

$$\begin{aligned} & \frac{\partial u}{\partial x} + \frac{\partial v}{\partial y} + \frac{\partial w}{\partial z} = 0 \\ & \rho \left(\frac{\partial u}{\partial t} + u \frac{\partial u}{\partial x} + v \frac{\partial u}{\partial y} + w \frac{\partial u}{\partial z} \right) = -\frac{\partial p}{\partial x} + \frac{\partial}{\partial x} \left(\mu \frac{\partial u}{\partial x} \right) + \frac{\partial}{\partial y} \left(\mu \frac{\partial u}{\partial y} \right) + \frac{\partial}{\partial z} \left(\mu \frac{\partial u}{\partial z} \right) + f_1 \\ & \rho \left(\frac{\partial v}{\partial t} + u \frac{\partial v}{\partial x} + v \frac{\partial v}{\partial y} + w \frac{\partial v}{\partial z} \right) = -\frac{\partial p}{\partial y} + \frac{\partial}{\partial x} \left(\mu \frac{\partial v}{\partial x} \right) + \frac{\partial}{\partial y} \left(\mu \frac{\partial v}{\partial y} \right) + \frac{\partial}{\partial z} \left(\mu \frac{\partial v}{\partial z} \right) + f_2 \\ & \rho \left(\frac{\partial w}{\partial t} + u \frac{\partial w}{\partial x} + v \frac{\partial w}{\partial y} + w \frac{\partial w}{\partial z} \right) = -\frac{\partial p}{\partial z} + \frac{\partial}{\partial x} \left(\mu \frac{\partial w}{\partial x} \right) + \frac{\partial}{\partial y} \left(\mu \frac{\partial w}{\partial y} \right) + \frac{\partial}{\partial z} \left(\mu \frac{\partial w}{\partial z} \right) + f_3 \end{aligned} \quad (33)$$

The external volume forces f_i are considered to be equal to 0 in this work. The equations (33) can be rewritten in conservative vector form

$$PW_t + F_x + G_y + H_z = R_x + S_y + T_z \quad (34)$$

which can be simplified for the two-dimensional case to

$$PW_t + F_x + G_y = R_x + S_y \quad (35)$$

where P is a diagonal matrix, the significance of which will be mentioned in 4.7. The vector W represents the unknowns, while F and G are the vectors for inviscid (convective) fluxes, and R and S are the vectors for viscous (diffusive) fluxes.

$$P = \text{diag}(0, 1, 1) \quad (36)$$

$$W = (p, u, v)^T \quad (37)$$

$$F = (u, u^2 + p, uv)^T \quad (38)$$

$$G = (v, uv, v^2 + p)^T \quad (39)$$

$$R = (0, \nu u_x, \nu v_x)^T \quad (40)$$

$$S = (0, \nu u_y, \nu v_y)^T \quad (41)$$

where ν is the kinematic viscosity defined as

$$\nu = \frac{\mu}{\rho} \quad (42)$$

Transformation into cylindrical coordinates We can express equations (33) given in Cartesian coordinates (x, y, z) in terms of the cylindrical coordinates (r, θ, x) using expressions

$$x = x \quad (43)$$

$$y = r \sin(\theta) \quad (44)$$

$$z = r \cos(\theta) \quad (45)$$

Continuity equation becomes

$$\frac{\partial u_r}{\partial r} + \frac{1}{r} \frac{\partial(r u_\theta)}{\partial \theta} + \frac{\partial u_x}{\partial x} = 0 \quad (46)$$

and momentum equations

$$\begin{aligned} & \rho \left(\frac{\partial u_r}{\partial t} + u_r \frac{\partial u_r}{\partial r} + \frac{u_\theta}{r} \frac{\partial u_r}{\partial \theta} + u_x \frac{\partial u_r}{\partial x} - \frac{u_\theta^2}{r} \right) = \\ & = -\frac{\partial p}{\partial r} + \mu \left[\frac{1}{r} \frac{\partial}{\partial r} \left(r \frac{\partial u_r}{\partial r} \right) + \frac{1}{r^2} \frac{\partial^2 u_r}{\partial \theta^2} + \frac{\partial^2 u_r}{\partial x^2} - \frac{u_r}{r^2} - \frac{2}{r^2} \frac{\partial u_\theta}{\partial \theta} \right] + f_1 \\ & \rho \left(\frac{\partial u_\theta}{\partial t} + u_\theta \frac{\partial u_\theta}{\partial r} + \frac{u_\theta}{r} \frac{\partial u_\theta}{\partial \theta} + u_x \frac{\partial u_\theta}{\partial x} - \frac{u_r u_\theta}{r} \right) = \\ & = -\frac{1}{r} \frac{\partial p}{\partial \theta} + \mu \left[\frac{1}{r} \frac{\partial}{\partial r} \left(r \frac{\partial u_\theta}{\partial r} \right) + \frac{1}{r^2} \frac{\partial^2 u_\theta}{\partial \theta^2} + \frac{\partial^2 u_\theta}{\partial x^2} - \frac{u_\theta}{r^2} + \frac{2}{r^2} \frac{\partial u_r}{\partial \theta} \right] + f_2 \\ & \rho \left(\frac{\partial u_x}{\partial t} + u_r \frac{\partial u_x}{\partial r} + \frac{u_\theta}{r} \frac{\partial u_x}{\partial \theta} + u_x \frac{\partial u_x}{\partial x} \right) = \\ & = -\frac{\partial p}{\partial x} + \mu \left[\frac{1}{r} \frac{\partial}{\partial r} \left(r \frac{\partial u_x}{\partial r} \right) + \frac{1}{r^2} \frac{\partial^2 u_x}{\partial \theta^2} + \frac{\partial^2 u_x}{\partial x^2} \right] + f_3 \end{aligned} \quad (47)$$

where u_r is radial velocity, u_θ is tangential velocity and u_x is axial velocity.

3.2.6 Analytical solution for N-S equations

Analytical solution for Navier-Stokes equations is also known as the Hagen–Poiseuille equation can be derived for the laminar flow through uniform pipe with radius R .

Assuming Navier-Stokes equations in three dimensional radial coordinates (r, θ, x) and steady, axisymmetric and fully developed flow with radial and azimuthal components of the fluid velocity equal to zero, we can simplify axial momentum equation to

$$\frac{1}{r} \frac{\partial}{\partial r} \left(r \frac{\partial u(r)}{\partial r} \right) = \frac{1}{\mu} \frac{\partial p}{\partial x} \quad (48)$$

where μ is dynamic viscosity of fluid.

We can now substitute

$$-\frac{\partial p}{\partial x} = \frac{p_2 - p_1}{L} = G \quad (49)$$

into (48) and integrate according to r to obtain

$$u(r) = -\frac{Gr^2}{4\mu} + A \ln r + B \quad (50)$$

In order for u to be finite at $r = 0$, we eliminate $A = 0$. To obtain constant B , we apply no-slip boundary condition $u(r = R) = 0$ and solve to get

$$B = \frac{GR^2}{4\mu} \quad (51)$$

We now get the solution for parabolic velocity profile in radial coordinates

$$u(r) = \frac{G}{4\mu} (R^2 - r^2) \quad (52)$$

Poiseuille flow To obtain Poiseuille flow between two infinitely long parallel plates, separated by a distance H with a constant pressure gradient

$$G = -\frac{\partial p}{\partial x} \quad (53)$$

we assume unidirectional flow in x direction. The Navier-Stokes equations then simplify to

$$\frac{\partial^2 u}{\partial y^2} = -\frac{G}{\mu} \quad (54)$$

By integrating twice, we obtain

$$u(y) = -\frac{G}{2\mu} y^2 + Ay + B \quad (55)$$

No slip boundary condition

$$u(0) = u(H) = 0 \quad (56)$$

we can get constants $B = 0$ and $A = \frac{G}{2\mu} H$ and the velocity profile

$$u(y) = -\frac{G}{2\mu} y(H - y) \quad (57)$$

3.2.7 Analytical solution for N-S equations for Power-law model fluids

We assume Navier-Stokes equations in three dimensional radial coordinates (r, θ, x) and steady, axisymmetric and fully developed flow with radial and azimuthal components of the fluid velocity equal to zero, we can simplify axial momentum equation to

$$\frac{\mu_{eff}}{r} \frac{\partial}{\partial r} \left(r \frac{\partial u(r)}{\partial r} \right) = \frac{\partial p}{\partial x} \quad (58)$$

where u is axial velocity in x -direction μ_{eff} is dynamic viscosity of fluid given by relation

$$\mu_{eff} = K \cdot \left| \frac{\partial u(r)}{\partial r} \right|^{\kappa-1} = K \cdot \dot{\gamma}^{\kappa-1} \quad (59)$$

where $\dot{\gamma}$ is the shear rate, K is the flow consistency index, and κ is the flow behavior index as described in 2.2. We can substitute μ_{eff} to obtain

$$\frac{1}{r} \frac{\partial}{\partial r} \left[K r \left(\frac{\partial u(r)}{\partial r} \right)^\kappa \right] = \frac{\partial p}{\partial x} \quad (60)$$

We assume

$$-\frac{\partial p}{\partial x} = \frac{p_2 - p_1}{L} = G \quad (61)$$

and integrate (60) with respect to r to obtain

$$K r \left(\frac{\partial u(r)}{\partial r} \right)^\kappa = G \frac{r^2}{2} + A \quad (62)$$

This equation can be rearranged to

$$\tau_{rx} = G \frac{r}{2} + \frac{A}{r} \quad (63)$$

and in order for τ_{rx} to be finite, we get $A = 0$. We can now write

$$\frac{\partial u(r)}{\partial r} = \left(\frac{G r}{K 2} \right)^{\frac{1}{\kappa}} \quad (64)$$

and integrate with respect to r to get equation

$$u(r) = \frac{\kappa}{\kappa + 1} \left(\frac{G}{2K} \right)^{\frac{1}{\kappa}} r^{\frac{\kappa+1}{\kappa}} + B \quad (65)$$

Applying no slip boundary condition $u(r = R) = 0$, we can express integration constant B as

$$B = -\frac{\kappa}{\kappa + 1} \left(\frac{G}{2K} \right)^{\frac{1}{\kappa}} R^{\frac{\kappa+1}{\kappa}} \quad (66)$$

Finally, we can write analytical solution for power law fluid as

$$u(r) = \frac{\kappa}{\kappa + 1} \left(\frac{G}{2K} \right)^{\frac{1}{\kappa}} \left(R^{\frac{\kappa+1}{\kappa}} - r^{\frac{\kappa+1}{\kappa}} \right) \quad (67)$$

Poiseuille flow To obtain Poiseuille flow of Power-law model fluid between two infinitely long parallel plates, separated by a distance H with a constant pressure gradient

$$G = -\frac{\partial p}{\partial x} \quad (68)$$

we assume unidirectional flow in x direction. The Navier-Stokes equations then simplify to

$$\frac{\partial}{\partial y} \left(\mu_{eff} \frac{\partial u}{\partial y} \right) = -G \quad (69)$$

where u is velocity in x -direction μ_{eff} is dynamic viscosity of fluid given by relation

$$\mu_{eff} = K \cdot \left(\frac{\partial u(y)}{\partial y} \right)^{\kappa-1} = K \cdot \dot{\gamma}^{\kappa-1} \quad (70)$$

where $\dot{\gamma}$ is the shear rate, K is the flow consistency index, and κ is the flow behavior index as described in 2.2.

We can substitute μ_{eff} to obtain

$$\frac{\partial}{\partial y} \left[K \cdot \left(\frac{\partial u}{\partial y} \right)^{\kappa} \right] = -G \quad (71)$$

By integrating with respect to y , we obtain

$$K \cdot \left(\frac{\partial u}{\partial y} \right)^{\kappa} = -Gy + A \quad (72)$$

which stands for shear stress τ_{xy} . Assuming the shear stress has to be zero at the axis of the channel, we can eliminate integral constant A . We can rearrange the equation as

$$\frac{\partial u}{\partial y} = \left(\frac{-Gy}{K} \right)^{\frac{1}{\kappa}} \quad (73)$$

and integrate again to obtain

$$u(y) = -\frac{\kappa}{\kappa+1} \frac{K}{G} \left(\frac{-Gy}{K} \right)^{\frac{1+\kappa}{\kappa}} + B \quad (74)$$

Using no slip boundary condition

$$u\left(\frac{H}{2}\right) = u\left(-\frac{H}{2}\right) = 0 \quad (75)$$

we can get constant

$$B = \frac{\kappa}{\kappa+1} \frac{K}{G} \left(\frac{-G\frac{H}{2}}{K} \right)^{\frac{1+\kappa}{\kappa}} \quad (76)$$

and the velocity profile is

$$u(y) = -\frac{\kappa}{\kappa+1} \left(\frac{G}{K} \right)^{\frac{1}{\kappa}} \left[\left(\frac{H}{2} \right)^{\frac{\kappa+1}{\kappa}} - y^{\frac{\kappa+1}{\kappa}} \right] \quad (77)$$

We can notice, using $\kappa = 1$ for flow behavior index in (77) leads to equation for velocity profile for Newtonian fluid as equation (57). [12]

3.2.8 Analytical solution for N-S equations under oscillating pressure

We consider homogenous, incompressible Newtonian fluid with density ρ and dynamic viscosity μ through circular tube with radius R with rigid walls. The flow is one-dimensional laminar and axisymmetric to the axis of the tube.

Navier-Stokes equation then becomes

$$\rho \frac{\partial u(r, t)}{\partial t} = -\frac{\partial p}{\partial x} + \mu \left(\frac{\partial^2 u(r, t)}{\partial r^2} + \frac{1}{r} \frac{\partial u(r, t)}{\partial r} \right) \quad (78)$$

and continuity equation

$$\frac{\partial u(r, t)}{\partial x} = 0 \quad (79)$$

where $u(r, t)$ represents velocity in x -direction and $\frac{\partial p}{\partial x}$ is the pressure gradient, periodic in time, defined as Fourier series

$$\frac{\partial p}{\partial x}(t) = \sum_{n=0}^N P'_n e^{in\omega t} \quad (80)$$

where ω is the angular frequency of the first harmonic $n = 1$ defined in Section 3.1.2, P'_n are the amplitudes of each harmonic n and $i = \sqrt{-1}$. P'_0 is the steady-state pressure gradient.

The velocity can be decomposed as Fourier series as

$$u(r, t) = \sum_{n=0}^N U_n e^{in\omega t} \quad (81)$$

where U_n are the amplitudes of each harmonic of the periodic function, and the steady component $n = 0$ refers to Poiseuille flow derived in 3.2.6

$$U_0 = -\frac{P'_0}{4\mu} (R^2 - r^2) \quad (82)$$

The Navier-Stokes equation for each harmonics can be written as

$$i\rho n\omega U_n = -P'_n + \mu \left(\frac{\partial^2 U_n}{\partial r^2} + \frac{1}{r} \frac{\partial U_n}{\partial r} \right) \quad (83)$$

The boundary condition is set as no-slip condition:

$$U_n(-R, t) = U_n(R, t) = 0 \quad (84)$$

for all t and axisymmetry

$$\frac{\partial U_n(0, t)}{\partial r} = 0 \quad (85)$$

For $n \geq 1$, we obtain general solution of this ordinary differential equation for the oscillatory part

$$U_n(r) = A_n J_0 \left(Wo \frac{r}{R} n^{1/2} i^{3/2} \right) + N_n Y_0 \left(Wo \frac{r}{R} n^{1/2} i^{3/2} \right) + \frac{iP'_n}{\rho n\omega} \quad (86)$$

where $J_0(\cdot)$ is the Bessel function of first kind and order zero, $Y_0(\cdot)$ is the Bessel function of second kind and order zero, A_n and B_n are arbitrary constants, and $Wo = R\sqrt{\frac{\omega \cdot \rho}{\mu}}$ is the dimensionless Womersley number defined in 3.1.2.

Applying axisymmetric boundary condition (85) $\frac{\partial u(0,t)}{\partial r} = 0$, we eliminate $B_n = 0$ as derivatives of Bessel functions $J'_0(\cdot)$ and $Y'_0(\cdot)$ approach infinity.

To obtain A_n , we apply no-slip boundary condition (84) resulting in

$$A_n = -\frac{iP'_n}{\rho n \omega} \frac{1}{J_0(Wo \cdot n^{1/2} i^{3/2})} \quad (87)$$

and thus the amplitudes of the velocity profile of the harmonic n becomes

$$U_n(r) = \frac{iP'_n}{\rho n \omega} \left[1 - \frac{J_0\left(\frac{Wo r}{R} n^{1/2} i^{3/2}\right)}{J_0(Wo \cdot n^{1/2} i^{3/2})} \right] \quad (88)$$

Velocity profile is obtained by taking the real part of the complex function resulted from the summation of all harmonics of the pulse as

$$u(r, t) = \frac{P'_0}{4\mu} (R^2 - r^2) + \text{Re} \left\{ \sum_{n=1}^N \frac{iP'_n}{\rho n \omega} \left[1 - \frac{J_0\left(\frac{Wo r}{R} n^{1/2} i^{3/2}\right)}{J_0(Wo \cdot n^{1/2} i^{3/2})} \right] e^{in\omega t} \right\} \quad (89)$$

Two dimensional case We consider Poiseuille flow with constant viscosity μ driven by oscillating pressure

$$-\frac{1}{\rho} \frac{\partial p}{\partial x} = -G - C \cos \omega t \quad (90)$$

where ω is angular frequency and C is the amplitude of pressure oscillation and G is steady pressure gradient. We will rewrite this equation in Fourier representation

$$-\frac{1}{\rho} \frac{\partial p}{\partial x} = -G - \text{Re}(C e^{i\omega t}) \quad (91)$$

We expect velocity as complex function

$$u = u_P + \text{Re}(U(\omega, y) e^{i\omega t}) \quad (92)$$

where u_P represents the Poiseuille solution for constant pressure gradient and U is amplitude of velocity. We can then write momentum equations as

$$\frac{\partial u}{\partial t} = -\frac{1}{\rho} \frac{\partial p}{\partial x} + \nu \frac{\partial^2 u}{\partial y^2} \quad (93)$$

and substituting for u and p

$$i\omega U = -C + \nu \frac{\partial^2 U}{\partial y^2} \quad (94)$$

For boundary conditions

$$\begin{aligned} U\left(\frac{H}{2}\right) &= 0 \\ \frac{\partial U}{\partial y}(0) &= 0 \end{aligned} \quad (95)$$

we can solve (94) as

$$U = \text{Re} \left[\frac{iC}{\omega} \left(1 - \frac{\cosh \sqrt{\frac{i\omega}{\nu}} y}{\cosh \sqrt{\frac{i\omega}{\nu}} \frac{H}{2}} \right) \right] \quad (96)$$

Using $\sqrt{i} = \frac{(1+i)}{\sqrt{2}}$, we obtain real part of (96)

$$u = u_P - \frac{C}{\omega} \left[\left(1 - \frac{f_1(\omega, y)}{f_3(k\frac{H}{2})} \right) \sin \omega t - \frac{f_2(\omega, y)}{f_3(k\frac{H}{2})} \cos \omega t \right], \quad (97)$$

where the various notations are defined as follows

$$\begin{aligned} k &= \sqrt{\frac{\omega}{2\nu}} \\ cc(\xi) &= \cos(\xi) \cosh(\xi) \\ ss(\xi) &= \sin(\xi) \sinh(\xi) \\ f_1(\omega, y) &= cc(ky)cc(kH) + ss(ky)ss(kH) \\ f_2(\omega, y) &= cc(ky)ss(kH) - ss(ky)cc(kH) \\ f_3(\omega) &= cc^2(\xi) + ss^2(\xi). \end{aligned}$$

In this case, Womersley number is $Wo = \frac{\sqrt{2}}{4}kH$.

Flow rate is obtained by integrating the velocity field on the cross-section and its derivation is further described in [22], [13], [15] or [16] as well as derivation of wall-shear stress. [7], [30]

4 Numerical model

The "Numerical Model" section represents a pivotal aspect of our research, enabling us to bridge theoretical insights with practical simulations. Among the various methods available, we have opted for the finite volume approach due to its proven effectiveness in simulating fluid dynamics.

Incorporating the finite volume method, we initiate our exploration by delving into its fundamental principles. This approach involves discretizing the computational domain into finite volumes or control volumes, each of which is evaluated to approximate the behavior of the fluid. This step involves breaking down the governing equations into discrete forms that can be solved numerically. This discretization paves the way for detailed simulations of fluid behavior.

The MacCormack scheme emerges as another key component of our numerical model. By embracing this two-step predictor-corrector approach, we unlock the potential to simulate complex fluid dynamics scenarios with improved accuracy.

We then delve into the discretization of both inviscid and viscous fluxes, essential steps in capturing the intricate interplay between flow properties.

We then investigate the artificial compressibility method. Simple method of coupling velocity and pressure.

Further, we describe another method of coupling velocity and pressure to be able to simulate cases with oscillating pressure.

While several methods exist for fluid dynamics simulations, our deliberate choice of the finite volume method arises from its proven suitability for our study. Its ability to capture the intricacies of fluid behavior, coupled with its compatibility with non-Newtonian fluids, positions us to unveil valuable insights into this complex realm.

4.1 Finite volume method

The finite volume method involves dividing the computational domain into a finite number of cells (control volumes) $D_{i,j}$, for which the integral form of the equations is used, allowing us to transform partial differential equations into a system of algebraic equations with a finite number of unknowns. Unlike the finite difference method, where the variable field is replaced by values at grid points, the finite volume method uses the average values for the given control volumes.

Its advantage lies in its simple application to general (non-orthogonal) grids, which can better mimic complex geometries but require more data organization.

4.2 Finite volumes method discretization

We can rewrite Equation (35) as

$$PW_t + (F - R)_x + (G - S)_y = 0 \quad (98)$$

After performing surface integration, we get

$$P \int_{D_{i,j}} W_t dS + \int_{D_{i,j}} [(F - R)_x + (G - S)_y] dS = 0 \quad (99)$$

We can use Green's theorem on the second integral

$$P \int_{D_{i,j}} W_t dS + \oint_{\partial D} [(F - R)dy - (G - S)dx] = 0 \quad (100)$$

Now, we can replace the vector of unknowns $W_{i,j} = \frac{1}{|D|} \int_D W dS$ with the average values of unknowns in the cell $D_{i,j}$ to obtain

$$P \frac{\partial W_{i,j}}{\partial t} + \frac{1}{|D|} \oint_{\partial D} [(F - R)dy - (G - S)dx] = 0 \quad (101)$$

4.3 MacCormack scheme

The MacCormack Scheme is a two-step scheme based on the two-stage Lax-Wendroff scheme and works on the predictor-corrector principle. In the first step, the predictor is computed, and the values obtained are used in the corrector, followed by adding the artificial viscosity term. Then next iterating step follows

Predictor

$$W_{i,j}^{n+\frac{1}{2}} = W_{i,j}^n - P^{-1} \frac{\Delta t}{|D_{i,j}|} \sum_{k=1}^4 [(F_k^n - R_k^n) \Delta y_k - (G_k^n - S_k^n) \Delta x_k] \quad (102)$$

Corrector + predictor

$$[W_{i,j}^{n+1}] = \frac{1}{2} \left(W_{i,j}^n + W_{i,j}^{n+\frac{1}{2}} - P^{-1} \frac{\Delta t}{|D_{i,j}|} \sum_{k=1}^4 \left[(F_k^{n+\frac{1}{2}} - R_k^{n+\frac{1}{2}}) \Delta y_k - (G_k^{n+\frac{1}{2}} - S_k^{n+\frac{1}{2}}) \Delta x_k \right] \right) \quad (103)$$

Corrector + predictor + artificial viscosity

$$W_{i,j}^{n+1} = [W_{i,j}^{n+1}] + DW_{i,j}^n \quad (104)$$

[26], [20]

4.4 Discretization of inviscid fluxes

Predictor

$$F_1 = F_2 = F_{i,j}, \quad F_3 = F_{i-1,j}, \quad F_4 = F_{i,j-1} \quad (105)$$

Corrector

$$F_1 = F_{i+1,j}, \quad F_2 = F_{i,j+1}, \quad F_3 = F_4 = F_{i,j} \quad (106)$$

Similarly for G ,

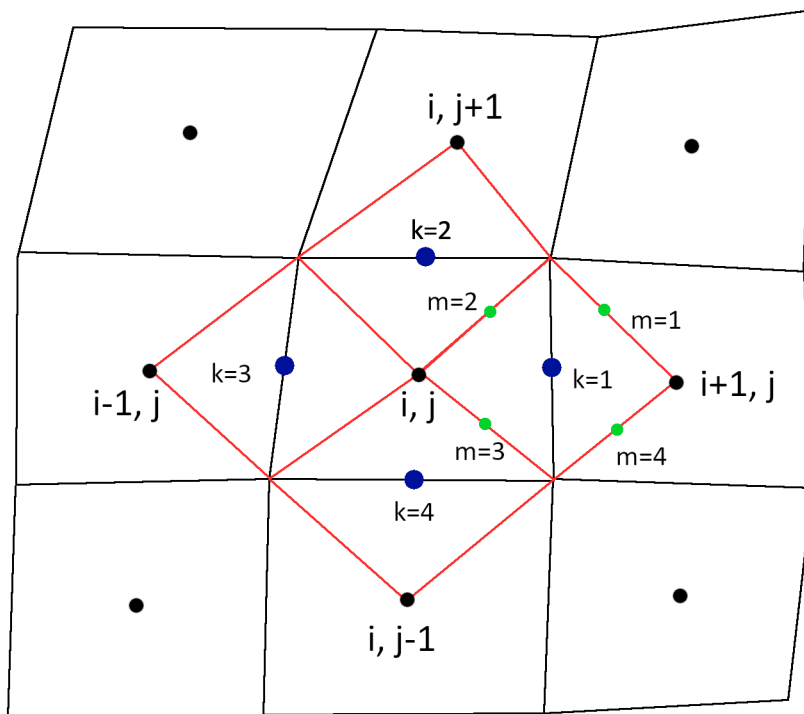


Figure 2: Stencil for Finite Volume Method computation

4.5 Discretization of viscous fluxes

The derivatives in velocities for viscous fluxes are obtained by integrating over the boundary of dual cells (indicated by the red boundary in Fig. 2).

$$u_x \approx \frac{1}{D_m} \oint_{\partial D} u v^x dl \quad (107)$$

And this integral can be replaced by a sum over the edges of dual cells:

$$u_x \approx \frac{1}{D_m} \sum_{m=1}^4 u_m v_m^x l_m \quad (108)$$

where u_m is the velocity at the center of the m -th edge, v_m^x is the unit outward normal of the edge, l_m is the length of the edge, and D_m is the area of the dual cell. The values of variables at the centers of dual cells are approximated as averages of neighboring values. [26]

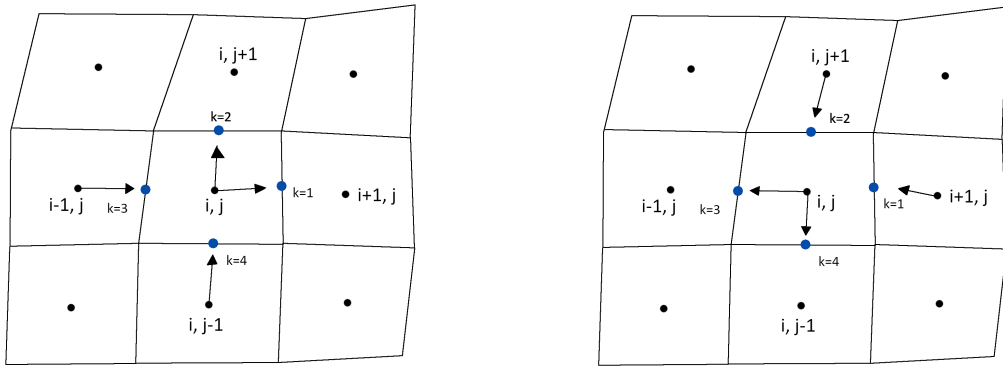
4.6 Discretization of pressure derivatives

The derivatives of pressure are obtained by integrating over the boundary of dual cells (indicated by the red boundary in Fig. 2).

$$p_x \approx \frac{1}{D_m} \oint_{\partial D} p v^x dl \quad (109)$$

And this integral can be replaced by a sum over the edges of dual cells:

$$p_x \approx \frac{1}{D_m} \sum_{m=1}^4 p_m v_m^x l_m \quad (110)$$



(a) Predictor

(b) Corrector

Figure 3: Stencil for computation of inviscid fluxes

where p_m is the pressure at the center of the m -th edge, ν_m^x is the unit outward normal of the edge, l_m is the length of the edge, and D_m is the area of the dual cell. The values of variables at the centers of dual cells are approximated as averages of neighboring values.

4.7 Artificial compressibility method

The artificial compressibility method allows us to add pressure p to the vector of unknowns for steady flow of incompressible fluid. By adding the time derivative of pressure to the continuity equation (18), we obtain the equation

$$\frac{1}{\beta^2} \frac{\partial p}{\partial t} + \frac{\partial u}{\partial x} + \frac{\partial v}{\partial y} = 0 \quad (111)$$

where β is the artificial compressibility coefficient representing the artificial sound speed. The added time derivative of pressure becomes zero for a steady solution. The system of equations (35) is then modified to:

$$\tilde{P}W_t + F_x + G_y = R_x + S_y \quad (112)$$

where

$$\tilde{P} = \begin{pmatrix} \frac{1}{\beta^2} & 0 & 0 \\ 0 & 1 & 0 \\ 0 & 0 & 1 \end{pmatrix} \quad (113)$$

The parameter β is recommended to be chosen as:

$$\beta = u_{\max} \cdot \sqrt{\rho} \quad (114)$$

where u_{\max} is the maximum velocity of the fluid and ρ is the fluid density.

4.8 Pressure equation

Using equations (32) and considering two dimensional case with outer forces f_i equal to zero

$$\begin{aligned} \nabla \cdot \mathbf{v} &= 0 \\ \frac{\partial \mathbf{v}}{\partial t} + (\mathbf{v} \cdot \nabla) \mathbf{v} &= -\frac{1}{\rho} \nabla p + \nu \nabla^2 \mathbf{v} \end{aligned} \quad (115)$$

we can rewrite the momentum equations in x and y components

$$\begin{aligned} \frac{\partial u}{\partial t} + u \frac{\partial u}{\partial x} + v \frac{\partial u}{\partial y} &= -\frac{1}{\rho} \frac{\partial p}{\partial x} + \nu \left(\frac{\partial^2 u}{\partial x^2} + \frac{\partial^2 u}{\partial y^2} \right) \\ \frac{\partial v}{\partial t} + u \frac{\partial v}{\partial x} + v \frac{\partial v}{\partial y} &= -\frac{1}{\rho} \frac{\partial p}{\partial y} + \nu \left(\frac{\partial^2 v}{\partial x^2} + \frac{\partial^2 v}{\partial y^2} \right) \end{aligned} \quad (116)$$

and continuity equation

$$\frac{\partial u}{\partial x} + \frac{\partial v}{\partial y} = 0 \quad (117)$$

We can rearrange the momentum equations, and derivate x -momentum equation with respect to x and y -momentum equation with respect to y to obtain

$$\begin{aligned}\frac{\partial^2 p}{\partial x^2} &= \rho \left[\nu \frac{\partial}{\partial x} (\Delta u) - \left(\frac{\partial}{\partial t} \left(\frac{\partial u}{\partial x} \right) + \frac{\partial u}{\partial x} \frac{\partial u}{\partial x} + u \frac{\partial^2 u}{\partial x^2} + \frac{\partial v}{\partial x} \frac{\partial u}{\partial y} + v \frac{\partial^2 u}{\partial x \partial y} \right) \right] \\ \frac{\partial^2 p}{\partial y^2} &= \rho \left[\nu \frac{\partial}{\partial y} (\Delta v) - \left(\frac{\partial}{\partial t} \left(\frac{\partial v}{\partial y} \right) + \frac{\partial u}{\partial y} \frac{\partial v}{\partial x} + u \frac{\partial^2 v}{\partial x \partial y} + \frac{\partial v}{\partial y} \frac{\partial v}{\partial y} + v \frac{\partial^2 v}{\partial y^2} \right) \right]\end{aligned}\quad (118)$$

To get Poisson equation, we sum equations (118) and use continuity equation to cancel terms equal to zero

$$\begin{aligned}\frac{\partial^2 p}{\partial x^2} + \frac{\partial^2 p}{\partial y^2} &= \rho \nu \left(\underbrace{\frac{\partial^2 u}{\partial x^2} \left(\frac{\partial u}{\partial x} + \frac{\partial v}{\partial y} \right)}_{=0} + \underbrace{\frac{\partial^2 v}{\partial y^2} \left(\frac{\partial u}{\partial x} + \frac{\partial v}{\partial y} \right)}_{=0} \right) - \underbrace{\frac{\partial}{\partial t} \left(\frac{\partial u}{\partial x} + \frac{\partial v}{\partial y} \right)}_{=0} - \\ &\quad - \frac{\partial u}{\partial x} \frac{\partial u}{\partial x} - 2 \frac{\partial v}{\partial x} \frac{\partial u}{\partial y} - \frac{\partial v}{\partial y} \frac{\partial v}{\partial y} - u \underbrace{\frac{\partial}{\partial x} \left(\frac{\partial u}{\partial x} + \frac{\partial v}{\partial y} \right)}_{=0} - v \underbrace{\frac{\partial}{\partial y} \left(\frac{\partial u}{\partial x} + \frac{\partial v}{\partial y} \right)}_{=0}\end{aligned}\quad (119)$$

which leaves us with

$$\frac{\partial^2 p}{\partial x^2} + \frac{\partial^2 p}{\partial y^2} = -\rho \left(\frac{\partial u}{\partial x} \frac{\partial u}{\partial x} + 2 \frac{\partial u}{\partial y} \frac{\partial v}{\partial x} + \frac{\partial v}{\partial y} \frac{\partial v}{\partial y} \right)\quad (120)$$

This equation is called Poisson equation and it is commonly written as

$$\Delta p = b\quad (121)$$

where b stands for right hand side of Poisson equation for pressure. [12]

4.9 Pressure correction method

Basic principle of pressure correction method stands in separation of calculation of pressure and velocity field. Using equations (32) and considering two dimensional incompressible flow with outer forces f_i equal to zero

$$\begin{aligned}\nabla \cdot \mathbf{v} &= 0 \\ \frac{\partial \mathbf{v}}{\partial t} + (\mathbf{v} \cdot \nabla) \mathbf{v} &= -\frac{1}{\rho} \nabla p + \nu \nabla^2 \mathbf{v}\end{aligned}\quad (122)$$

with unknowns \mathbf{v} and p .

To obtain pressure p , we are using (120) that is derived by using divergence of momentum equations as described in 4.8.

For simplicity, let us assume a backward Euler scheme with time step Δt , we obtain

$$\frac{\mathbf{v}^* - \mathbf{v}^n}{\Delta t} = -\nabla \cdot (\mathbf{v} \otimes \mathbf{v})^n - \frac{1}{\rho} \nabla p^n + \nu \Delta \mathbf{v}^n\quad (123)$$

and we can obtain intermediate velocity field \mathbf{v}^* , that does not fulfill the continuity equation. We apply pressure correction p' and velocity correction \mathbf{v}' to obtain values in new time step

$$\mathbf{v}^{n+1} = \mathbf{v}^* + \mathbf{v}', \quad p^{n+1} = p^* + p'\quad (124)$$

and then

$$\begin{aligned}\frac{\mathbf{v}^{n+1} - \mathbf{v}^n}{\Delta t} &= -\nabla \cdot (\mathbf{v} \otimes \mathbf{v})^n - \frac{1}{\rho} \nabla p^{n+1} + \nu \Delta \mathbf{v}^n \\ \nabla \mathbf{v}^{n+1} &= 0\end{aligned}\quad (125)$$

To obtain equation for velocity correction, we substitute (124) to (123)

$$\frac{\mathbf{v}^{n+1} - \mathbf{v}' - \mathbf{v}^n}{\Delta t} = -\nabla \cdot (\mathbf{v} \otimes \mathbf{v})^n - \frac{1}{\rho} \nabla (p^{n+1} - p') + \nu \Delta \mathbf{v}^n \quad (126)$$

and subtracting first equation of (125), we are left with

$$\mathbf{v}' = -\frac{\Delta t}{\rho} \nabla p' \quad (127)$$

Using velocity correction, continuity equation becomes

$$\nabla \cdot (\mathbf{v}^* + \mathbf{v}') = 0 \quad (128)$$

and using (127)

$$\nabla \cdot \left(\mathbf{v}^* - \frac{\Delta t}{\rho} \nabla p' \right) = 0 \quad (129)$$

We can then express pressure correction as

$$\Delta p' = \frac{\rho}{\Delta t} \nabla \cdot \mathbf{v}^* \quad (130)$$

Discretization Left hand side of the equation (130) can be expressed as

$$\Delta p' \approx \frac{1}{|D_{i,j}|} \sum_{k=1}^4 [p'_{x,k} \Delta y_k - p'_{y,k} \Delta x_k] \quad (131)$$

where p'_x and p'_y is obtained using same method as described in Section 4.6, but using pressure corrections p' instead of actual pressure p and index k refers to faces of spatial discretization.

Right hand side can be expressed as

$$\frac{\rho}{\Delta t} \nabla \cdot \mathbf{v}^* \approx \frac{\rho}{\Delta t |D_{i,j}|} \sum_{k=1}^4 [u_k^* \Delta y_k - v_k^* \Delta x_k] \quad (132)$$

To obtain pressure correction in time n , we add term $\frac{p'^{\phi+1} - p'^{\phi}}{\Delta \tau}$ to left hand side, where τ is computational pseudotime and index ϕ refers to this pseudotime. This term should approach zero, as our solution approaches to correct pressure field. We get the equation for pressure correction as

$$\frac{p'^{\phi+1} - p'^{\phi}}{\Delta \tau} + \frac{1}{|D_{i,j}|} \sum_{k=1}^4 [p'_{x,k} \Delta y_k - p'_{y,k} \Delta x_k] = \frac{\rho}{\Delta t |D_{i,j}|} \sum_{k=1}^4 [u_k^* \Delta y_k - v_k^* \Delta x_k] \quad (133)$$

and rearranging to

$$p'^{\phi+1} = p'^{\phi} + \frac{\rho \Delta \tau}{\Delta t |D_{i,j}|} \sum_{k=1}^4 [u_k^* \Delta y_k - v_k^* \Delta x_k] - \frac{\Delta \tau}{|D_{i,j}|} \sum_{k=1}^4 [p'_{x,k} \Delta y_k - p'_{y,k} \Delta x_k] \quad (134)$$

4.9.1 Solving algorithm for pressure correction method

We start with pressure field from previous iteration with updated boundary condition to calculate intermediate velocity field \mathbf{v}^* in a form

$$\begin{aligned} u^* &= u^n - \frac{\Delta t}{|D_{i,j}|} \sum_{k=1}^4 [((u_k^n)^2 + p_k^n - \nu(u_{x,k}^n)) \Delta y_k - ((u_k^n v_k^n) - \nu(u_{y,k}^n)) \Delta x_k] \\ v^* &= v^n - \frac{\Delta t}{|D_{i,j}|} \sum_{k=1}^4 [((u_k^n v_k^n) - \nu(v_{x,k}^n)) \Delta y_k - ((v_k^n)^2 + p_k^n - \nu(v_{y,k}^n)) \Delta x_k] \end{aligned} \quad (135)$$

We use intermediate velocities to express equation for pressure correction as

$$p'^{\phi+1} = p'^{\phi} + \frac{\rho \Delta \tau}{\Delta t |D_{i,j}|} \sum_{k=1}^4 [u_k^* \Delta y_k - v_k^* \Delta x_k] - \frac{\Delta \tau}{|D_{i,j}|} \sum_{k=1}^4 [p'_{x,k}{}^{\phi} \Delta y_k - p'_{y,k}{}^{\phi} \Delta x_k] \quad (136)$$

We repeatedly solve this equation until term $\frac{p'^{\phi+1} - p'^{\phi}}{\Delta \tau}$ approaches desired accuracy. We then adjust pressure field using p' and calculate velocity correction using pressure correction and then adjust velocity field. This velocity field should fulfill continuity equation to a desired level and we step into another real time step. To approximate values at boundaries of cells, we use average between two neighboring cells and for simplicity, we use $\Delta t = \Delta \tau$.

5 Numerical experiments

5.1 Used geometries

Three different geometries are being used:

Straight channel This geometry is mainly used for validation as we are able to obtain analytical solution for steady flow of Newtonian and non-Newtonian fluid (see Section 3.2.6 and 3.2.7). Its dimensions should still resemble a larger vein in human body, therefore length in x -direction is set as $L = 25 \cdot 10^{-3} m$ and distance of the walls in y -direction resemble diameter of the vein and is given as $H = 5 \cdot 10^{-3} m$. Example of mesh with 50 cells in both directions can be seen in Fig. 4.

Stenosed channel Initial dimensions are same as in case of straight channel, resembling larger vein in human body, only the middle $\frac{1}{5}$ is gradually compressed to 0.7 of its original diameter using *cosine* function, simulating stenosis of vein. In this case

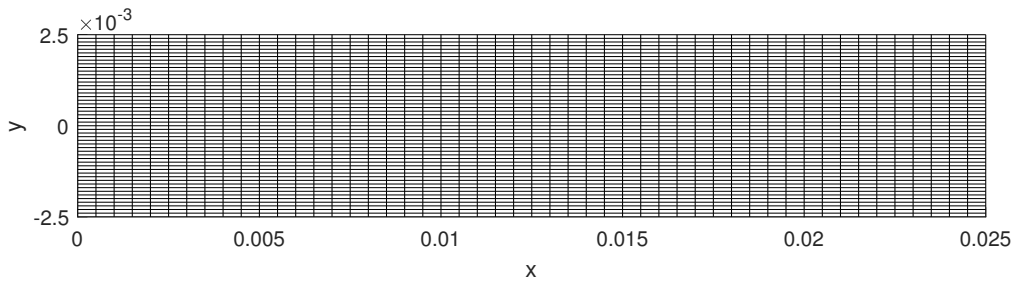


Figure 4: Mesh of straight channel with 50 cells in both directions

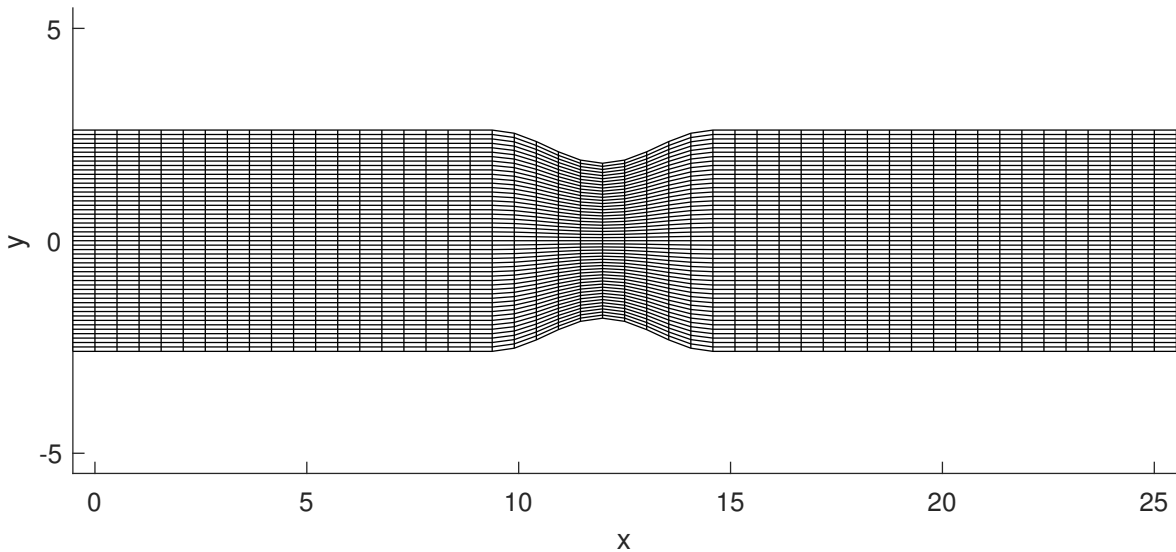


Figure 5: Mesh of stenosed channel with 50 cells in both directions

we expect higher velocities in stenosed part as well as flow in y -direction. Example of mesh with 50 cells in both directions can be seen in Fig. 5.

Curved channel Example of mesh for curved channel with 50 cells in both directions can be seen in Fig. 6.

5.2 Validation of artificial compressibility method for oscillating pressure gradient

In this section, we aim to compare the analytical solution obtained for the flow between two parallel plates, as described in Section 3.2.8, with the numerical simulation using the artificial compressibility method. The numerical simulation is conducted on a mesh depicted in Fig. 4, and the pressure gradient at the inlet is set as follows:

$$\delta p = 4.08 \cdot (1 + 0.2 \cdot \sin(2\pi \cdot (7/6) \cdot t)) \quad (137)$$

where t represents the current time in the simulation. Visual representation can be seen in Fig. 7.

To closely resemble the behavior of blood, the simulated fluid properties are set as follows: density $\rho = 1060$, $kg \cdot m^{-3}$, viscosity $\nu = 3 \cdot 10^{-6} m^2/s$, artificial compressibility

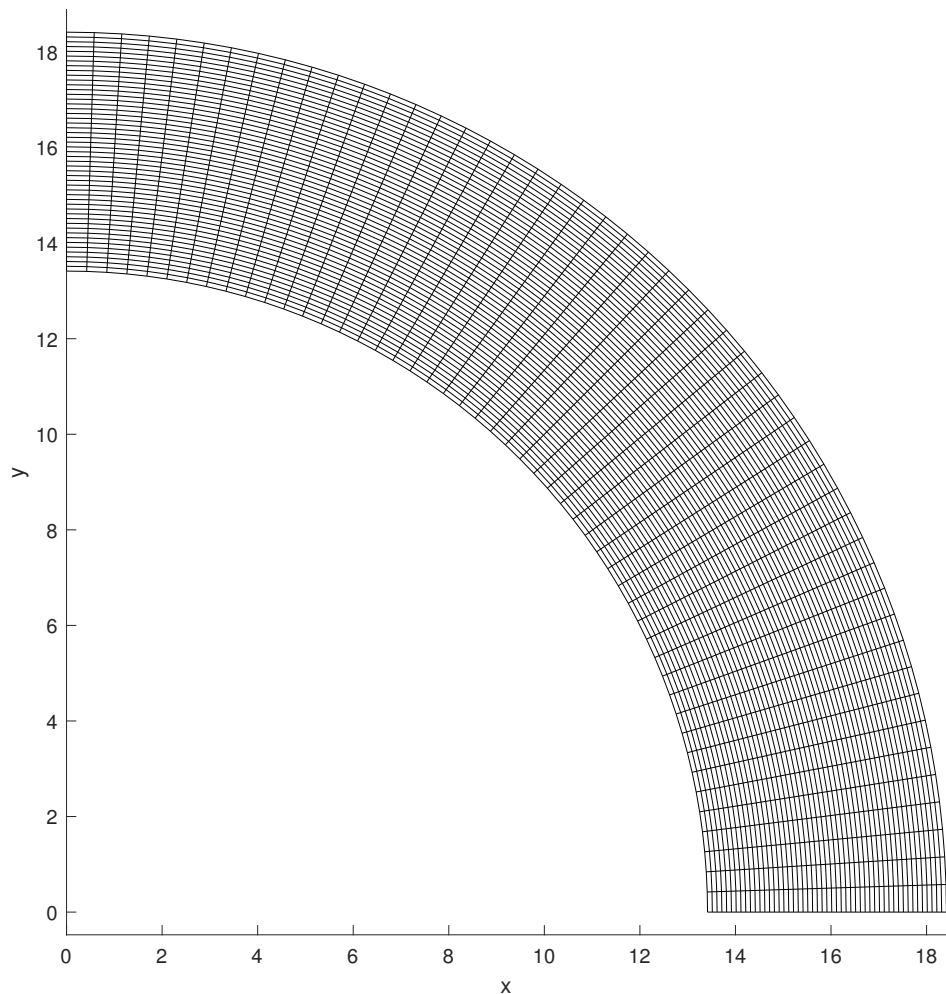


Figure 6: Mesh of curved channel with 50 cells in both directions

coefficient $\beta^2 = 1060$, and the time step $\Delta t = 2 \cdot 10^{-5} s$.

In order to quantify the difference between the analytical and numerical solutions, we will utilize the Euclidean norm of the difference between the two velocity fields. The Euclidean norm is defined as follows:

$$\|\mathbf{v}_{\text{analytical}} - \mathbf{v}_{\text{numerical}}\|_2 = \frac{1}{N} \left(\sum_{i=1}^N \left(v_{\text{analytical}}^{(i)} - v_{\text{numerical}}^{(i)} \right)^2 \right)^{\frac{1}{2}}$$

where $\mathbf{v}_{\text{analytical}}$ and $\mathbf{v}_{\text{numerical}}$ represent the velocity fields of the Newtonian and non-Newtonian fluids, respectively. The terms $v_{\text{analytical}}^{(i)}$ and $v_{\text{numerical}}^{(i)}$ denote the velocity components at each grid point or spatial location, and N represents the total number of cells. This normalization ensures that the results of the norm remain independent of the chosen grid size.

For given values

$$\begin{aligned} r &= 2.5 \cdot 10^{-3} m \\ \nu &= 3 \cdot 10^{-6} m^2/s \\ \omega &= \frac{7}{3} \pi rad/s \end{aligned} \tag{138}$$

The Womersley number can be calculated as follows:

$$Wo = r \cdot \sqrt{\frac{\omega}{\nu}} = 2.5 \cdot 10^{-3} \sqrt{\frac{\frac{7}{3} \pi}{3 \cdot 10^{-6}}} \approx 3.91 \tag{139}$$

The value of the Womersley number, approximately 3.91, corresponds to the renal artery according to the table 2.

In Fig. 8, we present the Euclidean norm of the difference between the analytical and numerical solutions obtained through simulation over seven periods, ending at $t = 6$ seconds. In the initial stages of the simulation, there is a decrease in the error due to the

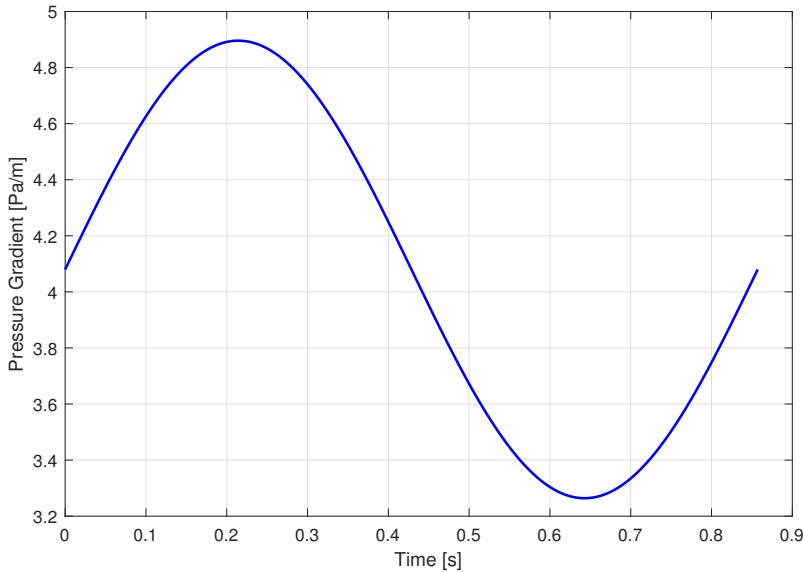


Figure 7: One period of pressure gradient

influence of unrealistic initial conditions. However, this initial error reduction stabilizes after the third period of simulation, where the error becomes periodic, depending on the pressure gradient set on the inlet. The maximal error observed after third period is $0.5 \cdot 10^{-3}$, indicating that the numerical solution closely approximates the analytical solution with a high level of accuracy.

In Fig. 9, we see pressure fields for several notable times on sine wave in last period of simulation. We don't see any unusual behavior compared to the simulation with constant pressure. We can note the pressure is equally distributed along the y -axis from the initial value set at the inlet δp to the 0 set on the outlet.

Values of velocity in the y -direction show a steady and expected behavior. Initially, they drop to around 10^{-6} during the first period and gradually decrease and stabilize at values close to 10^{-14} in the last three periods. This behavior is in line with our expectations for flow in only one direction, and it indicates that the flow is well-established.

The most crucial aspect to analyze is the velocity in the x -direction, as depicted in Fig. 10 for various notable times. From the comparison between the numerical simulation and the analytical solution, we observe that the numerical results closely match the analytical solution at times '3', '4', '7', and '8', which corresponds to data shown in Fig. 8. However, it is essential to note that throughout the simulation, there is a slight delay in the numerical results compared to the analytical solution. This delay becomes more prominent during larger pressure gradient shifts between time steps, resulting in higher discrepancies between the analytical and numerical solutions at times '1', '2', '5', and '6'.

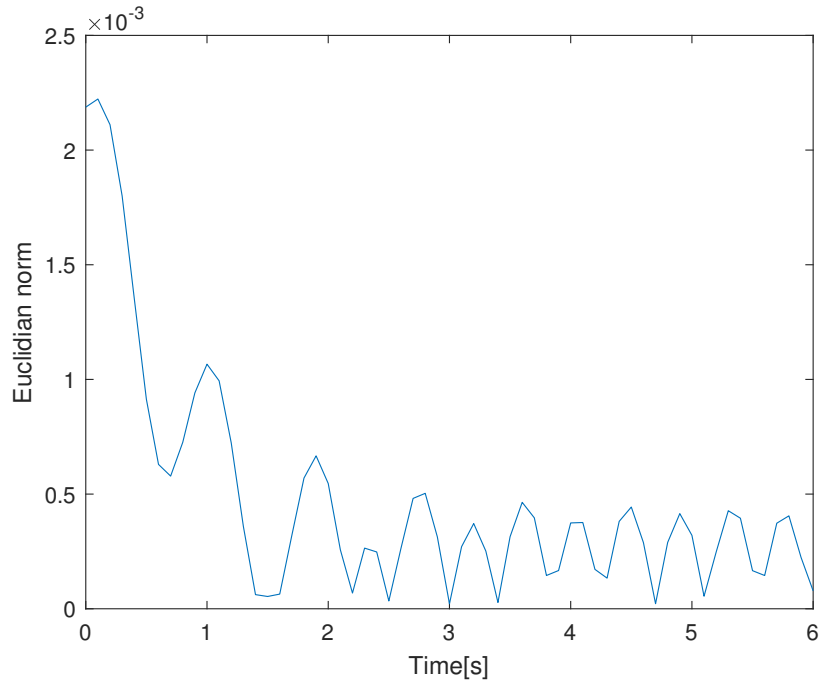
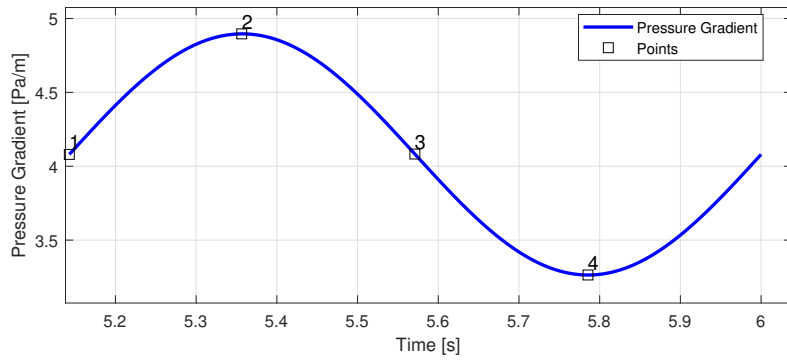
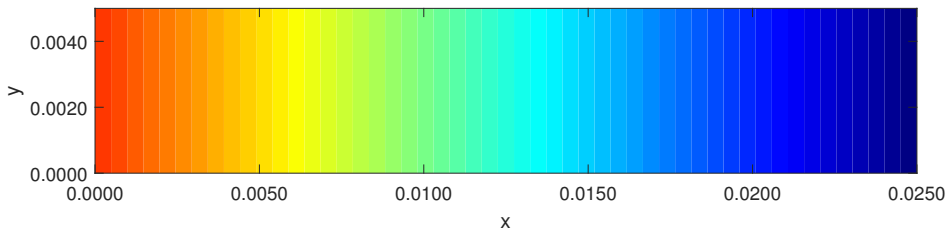


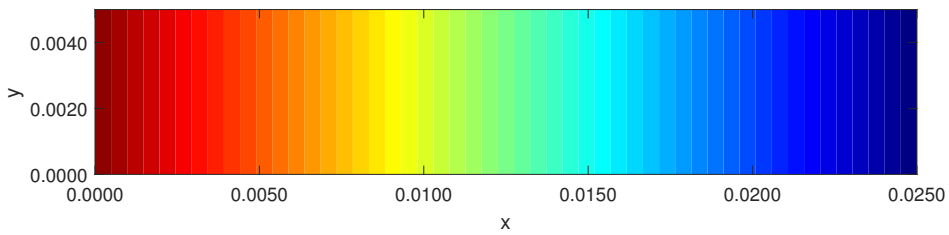
Figure 8: Euclidian norm of difference between analytical and numerical solution



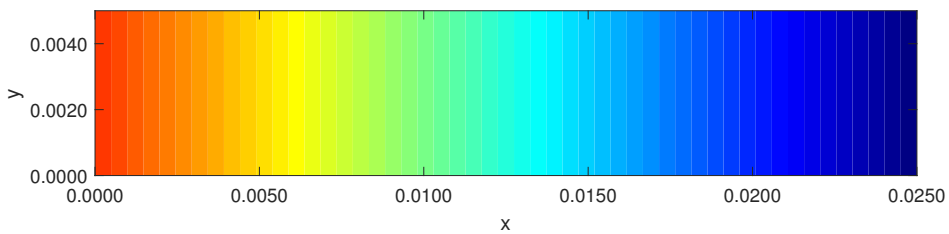
(a) Pressure on inlet and important time instants



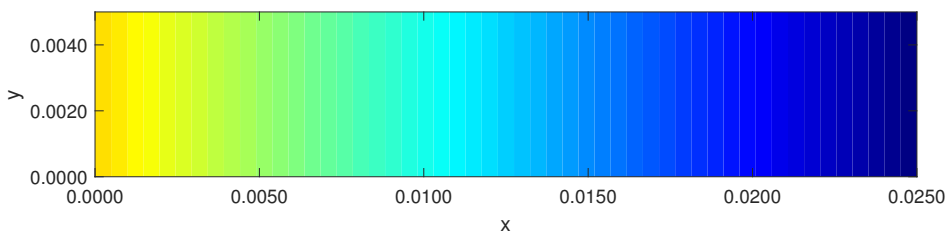
(b) Pressure field in time 1



(c) Pressure field in time 2



(d) Pressure field in time 3



(e) Pressure field in time 4

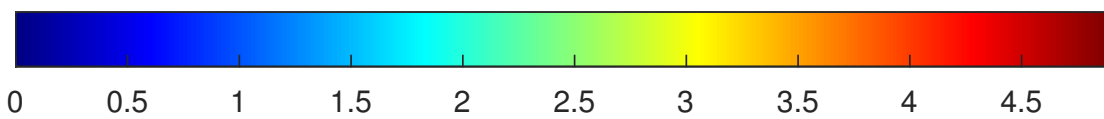
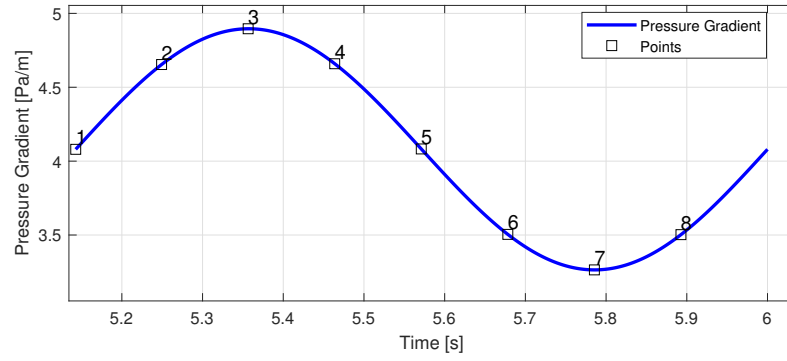
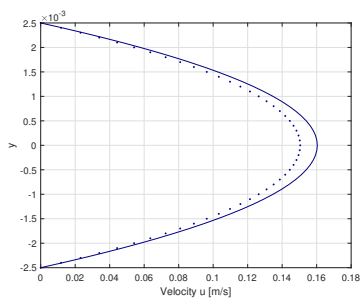


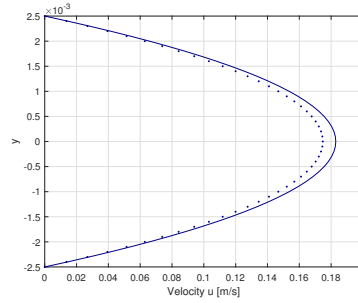
Figure 9: Pressure fields for different time instants of pressure sine in last period



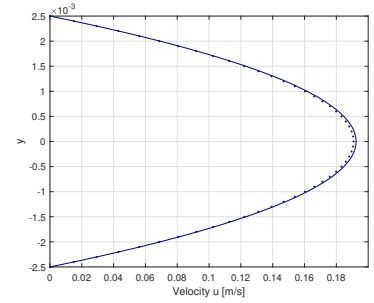
(a) Pressure on inlet and important time instants



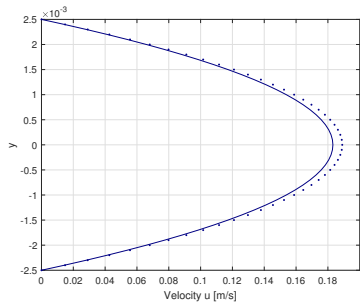
(b) Velocity u in time 1



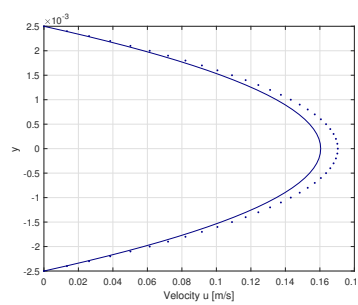
(c) Velocity u in time 2



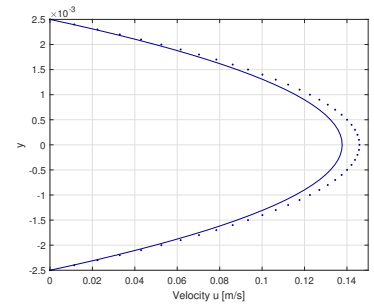
(d) Velocity u in time 3



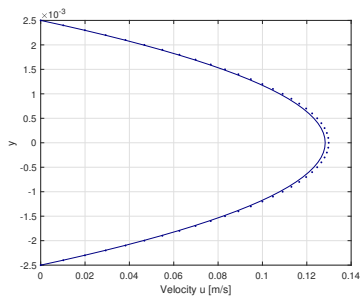
(e) Velocity u in time 4



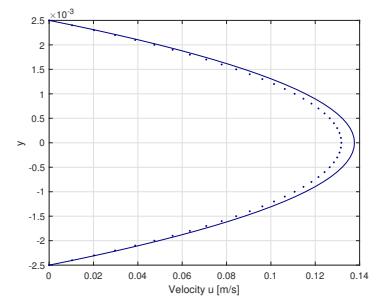
(f) Velocity u in time 5



(g) Velocity u in time 6



(h) Velocity u in time 7



(i) Velocity u in time 8

Figure 10: Horizontal velocity profiles for different time instants of pressure sine in last period

5.2.1 Conclusion

The pressure correction method offers a straightforward implementation and can effectively simulate the flow between two plates driven by oscillating pressure. However, it may encounter challenges in accurately capturing rapid shifts in pressure, leading to delayed velocity fields compared to the analytical solution. To enhance the method's performance, several improvement strategies can be considered, including the implementation of dual time stepping, exploration of alternative choices for the artificial compressibility coefficient, and other innovative approaches.

Dual time stepping, as a potential enhancement, introduces an additional time step that is significantly smaller than the main time step used for advancing the solution. By doing so, the method can better handle fast transient behavior and reduce numerical errors stemming from abrupt pressure changes. Such an adaptation may enhance the stability and accuracy of the simulation, particularly in situations with rapidly varying pressures. While this method may not prioritize absolute accuracy, speed remains a key advantage.

In conclusion, the pressure correction method holds promise for simulations with oscillating pressure, particularly when speed is of utmost importance. By incorporating dual time stepping, judiciously selecting the artificial compressibility coefficient, and considering other enhancement approaches, the method's performance can be notably improved to better handle shifts in pressure and achieve results closer to the analytical solution.

5.3 Validation of pressure corrections method for oscillating pressure gradient

In this section, we aim to compare the analytical solution obtained for the flow between two parallel plates, as described in Section 3.2.8, with the numerical simulation using the pressure correction method. Setting of the numerical simulation is similar to validation of artificial compressibility method. The numerical simulation is conducted on a mesh depicted in Fig. 4, and the pressure gradient at the inlet is set as follows:

$$\delta p = 4.08 \cdot (1 + 0.2 \cdot \sin(2\pi \cdot (7/6) \cdot t)) \quad (140)$$

where t represents the current time in the simulation. Visual representation can be seen in Fig. 7.

To closely resemble the behavior of blood, the simulated fluid properties are set as follows: density $\rho = 1060 \text{ kg} \cdot \text{m}^{-3}$, viscosity $\nu = 3 \cdot 10^{-6} \text{ m}^2/\text{s}$ and the time step $dt = 2 \cdot 10^{-5} \text{ s}$. Moreover, pressure will be corrected, until the value of divergence will be smaller than 10^{-6} or 100 times.

For given values

$$\begin{aligned} r &= 2.5 \cdot 10^{-3} \text{ m} \\ \nu &= 3 \cdot 10^{-6} \text{ m}^2/\text{s} \\ \omega &= \frac{7}{3}\pi \text{ rad/s} \end{aligned} \quad (141)$$

The Womersley number can be calculated as follows:

$$Wo = r \cdot \sqrt{\frac{\omega}{\nu}} = 2.5 \cdot 10^{-3} \sqrt{\frac{\frac{7}{3}\pi}{3 \cdot 10^{-6}}} \approx 3.91 \quad (142)$$

The value of the Womersley number, approximately 3.91, corresponds to the renal artery according to the table 2. In Fig. 11, we present the Euclidean norm of the difference between the analytical and numerical solutions obtained through simulation over seven periods, ending at $t = 6$ seconds. In the initial stages of the simulation, there is a decrease in the error due to the influence of unrealistic initial conditions. However, this initial error reduction stabilizes after the second period of simulation, where the error becomes periodic, depending on the pressure gradient set on the inlet. The maximal error observed after second period is $4 \cdot 10^{-6}$, indicating that the numerical solution closely approximates the analytical solution with a high level of accuracy. Compared to simulation using artificial compressibility method, pressure corrections method converges faster to the solution and shows more accurate solution.

In Fig. 12, we see pressure fields for several notable times on sine wave in last period of simulation. We don't see any unusual behavior compared to the simulation using artificial compressibility method with constant pressure nor oscillating pressure. We can note the pressure is equally distributed along the y -axis from the initial value set at the inlet δp to the 0 set on the outlet.

Values of velocity in the y -direction show a steady and expected behavior. Initially, they drop to around 10^{-9} during the first period and gradually decrease and stabilize at values close to 10^{-15} in the last four periods. This behavior is in line with our expectations for flow in only one direction, and it indicates that the flow is well-established.

The most crucial aspect to analyze is the velocity in the x -direction, as depicted in Fig. 13 for various notable times. From the comparison between the numerical simulation and the analytical solution, we observe that the numerical results closely match the analytical solution and although the difference between analytical solution and numerical solution can be seen, it seems consistent in all velocity profiles

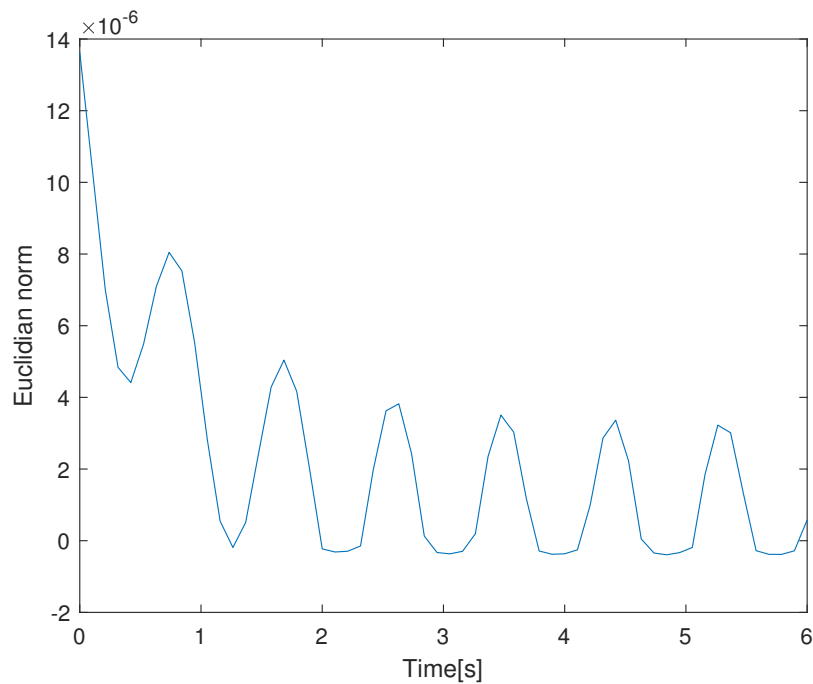
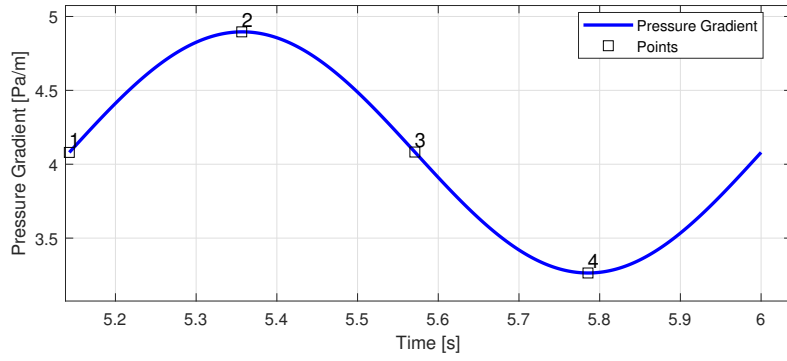
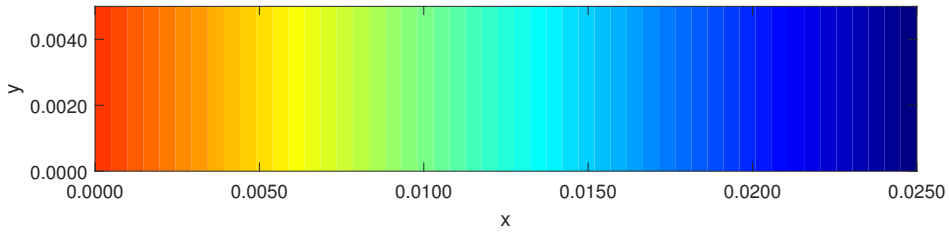


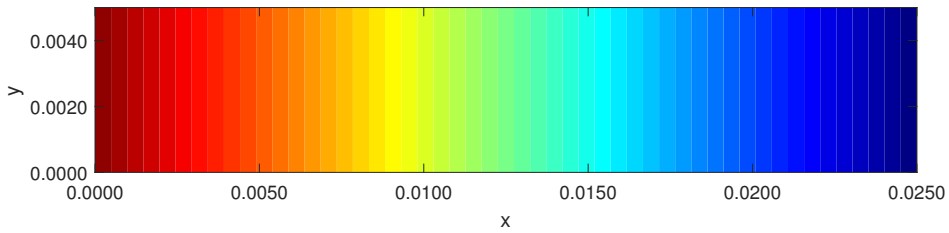
Figure 11: Euclidian norm of difference between analytical and numerical solution



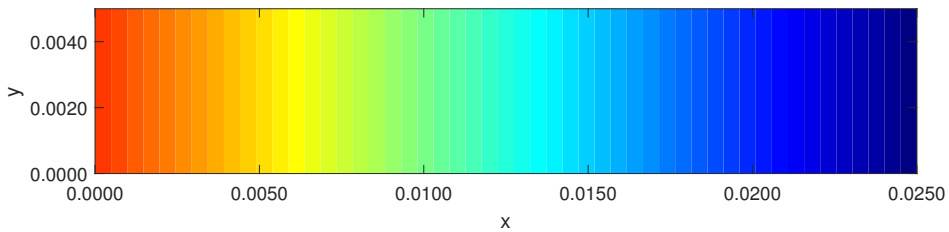
(a) Pressure on inlet and important time instants



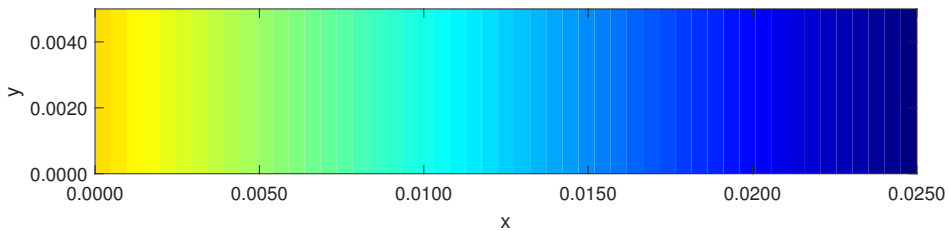
(b) Pressure field in time 1



(c) Pressure field in time 2



(d) Pressure field in time 3



(e) Pressure field in time 4

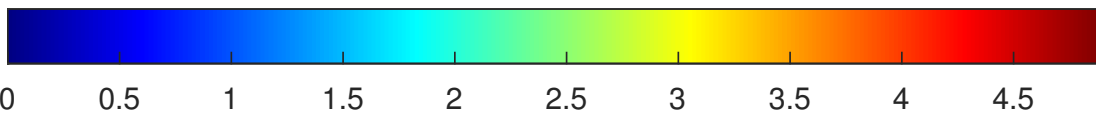
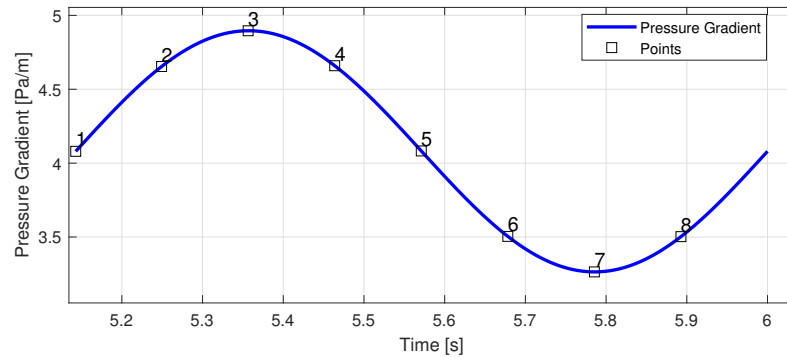
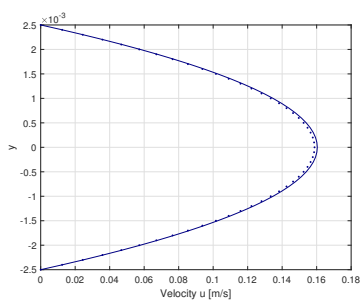


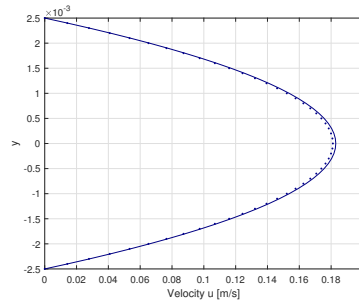
Figure 12: Pressure fields for different time instants of pressure sine in last period



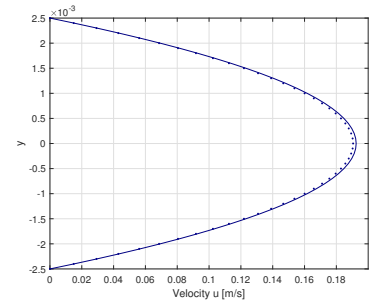
(a) Pressure on inlet and important time instants



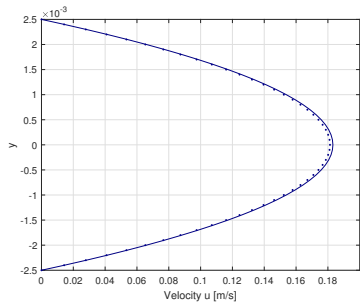
(b) Velocity u in time 1



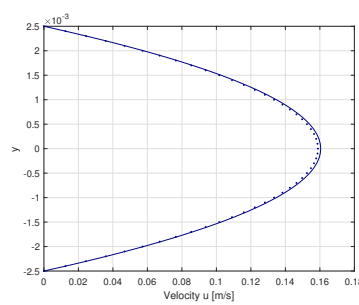
(c) Velocity u in time 2



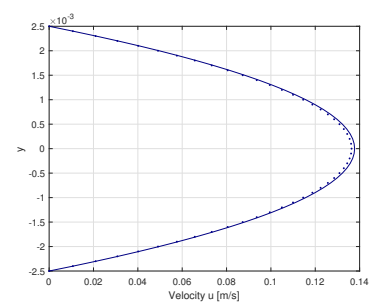
(d) Velocity u in time 3



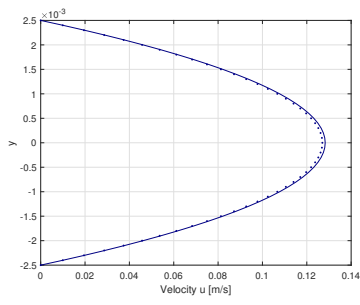
(e) Velocity u in time 4



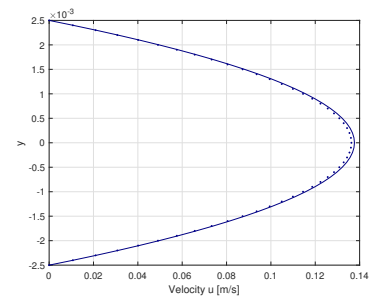
(f) Velocity u in time 5



(g) Velocity u in time 6



(h) Velocity u in time 7



(i) Velocity u in time 8

Figure 13: Horizontal velocity profiles for different time instants of pressure sine in last period

5.3.1 Conclusion

The pressure correction method presents a viable option for simulating the flow between two plates driven by oscillating pressure, particularly when dealing with fluid properties similar to blood. Notably, this method yields more accurate results compared to simulations using the artificial compressibility method. The higher precision in capturing the flow behavior makes it a preferred choice in scenarios where accuracy is of paramount importance.

However, it is essential to acknowledge that the pressure correction method demands a more involved implementation in code. Furthermore, the precision achieved by the pressure correction method comes at the cost of increased computational time. In comparison, simulations conducted using the artificial compressibility method demonstrate substantially faster execution, taking only about one-fifth of the time required by the pressure correction method.

Given the trade-off between accuracy and computational efficiency, the choice between the two methods depends on the specific requirements of the simulation. For applications where utmost precision is critical, the pressure correction method is the recommended approach despite the longer computational time. On the other hand, if computational speed is a priority and the level of accuracy can be compromised to some extent, the artificial compressibility method may be the more suitable option.

Ultimately, the decision should be based on the specific objectives of the simulation and the available computational resources. It is crucial to evaluate the benefits and limitations of each method carefully to ensure that the chosen approach aligns with the goals of the study and meets the desired level of accuracy and efficiency.

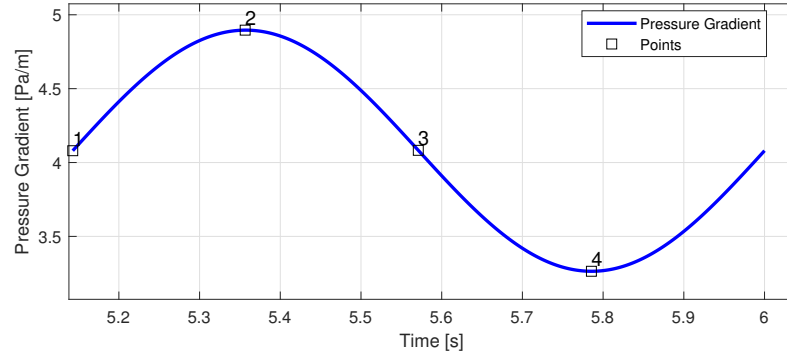
5.4 Simulation driven by oscillating pressure in stenosed channel

This simulation serves as a demonstration of the pressure corrections method solver's capability to handle scenarios involving irregular geometries and its comparison with solver using artificial compressibility method. The same initial conditions and settings as those employed in the validation case were utilized. The objective was to simulate blood behavior through a stenosed vein, where the geometry gradually narrows in middle $\frac{1}{5}$ to 0.7 of its original diameter, adopting a cosine function profile as detailed in Section 5.1. In this particular geometry, we anticipate flow acceleration within the constriction region and the emergence of velocity in the y -direction.

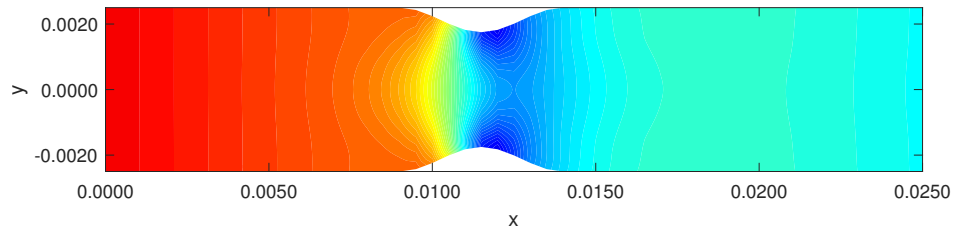
5.4.1 Results for oscillating pressure in stenosed channel

Fig. 14 illustrates the pressure distribution within the stenosed channel at various time points during the final period of the simulation under oscillating pressure conditions computed by solver using pressure corrections method. Notably, the pressure drop within the constricted region of the geometry is observable, akin to the findings observed in the simulation with constant pressure. This alignment in pressure behavior underscores the solver's consistent performance across varying pressure scenarios.

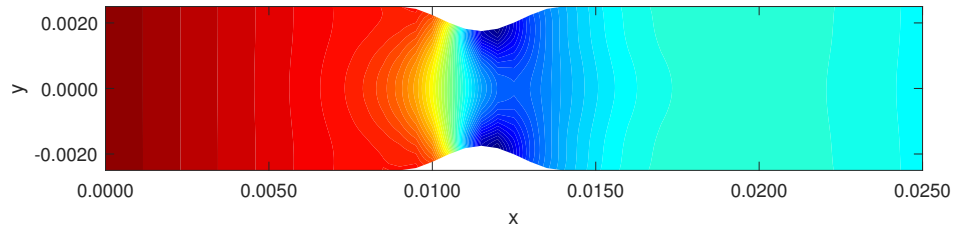
Fig. 15 presents the horizontal velocity u at corresponding time points for both solvers. Consistent with the simulation conducted under steady pressure conditions at the inlet, an evident augmentation in velocity emerges within the constricted region. This localized alteration in velocity propagates to the inlet and outlet sections, inducing



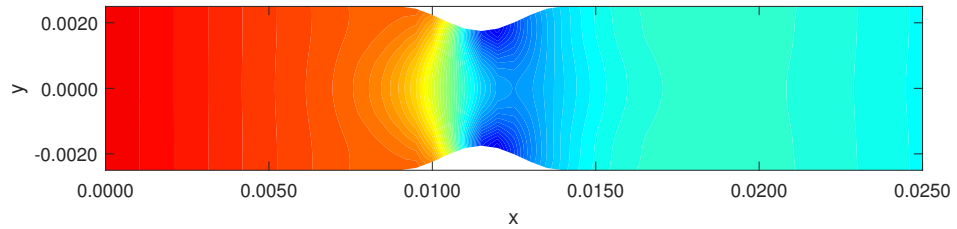
(a) Pressure on inlet and important time instants



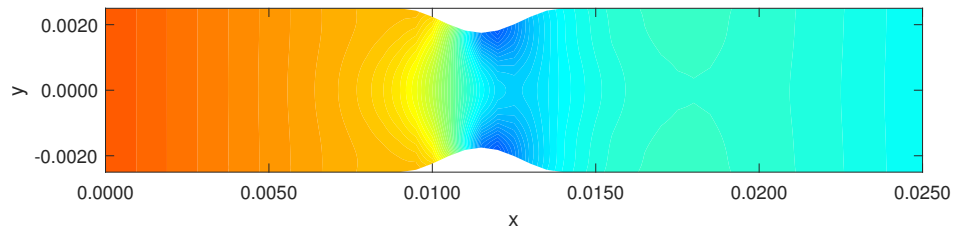
(b) Pressure field in time 1



(c) Pressure field in time 2



(d) Pressure field in time 3



(e) Pressure field in time 4

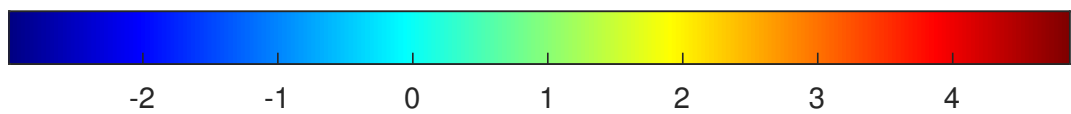


Figure 14: Pressure fields for different time instants of pressure sine in last period for stenosed channel

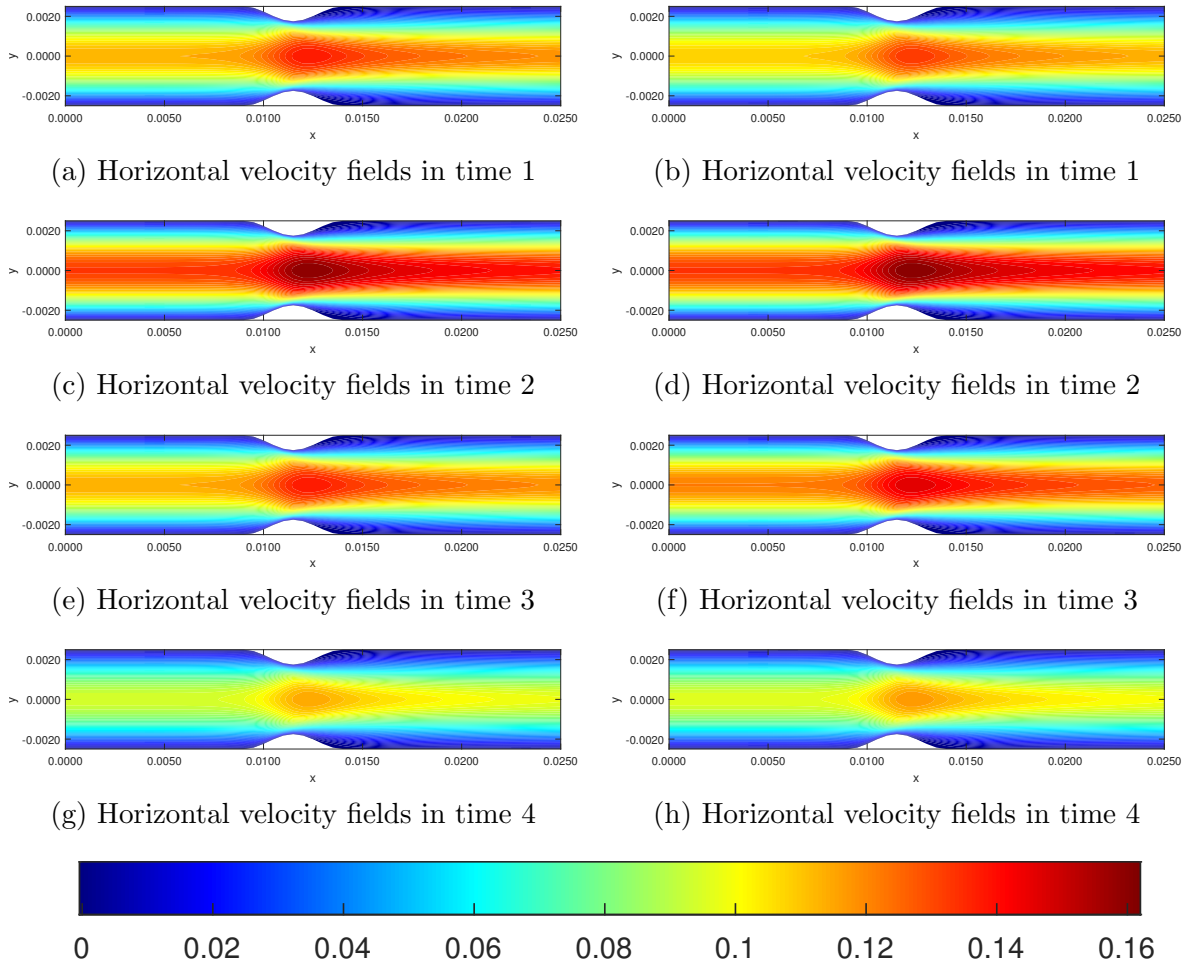


Figure 15: Horizontal velocity u fields for different time instants of pressure sine in last period for stenosed channel for pressure correction method on left, for artificial compressibility method on right

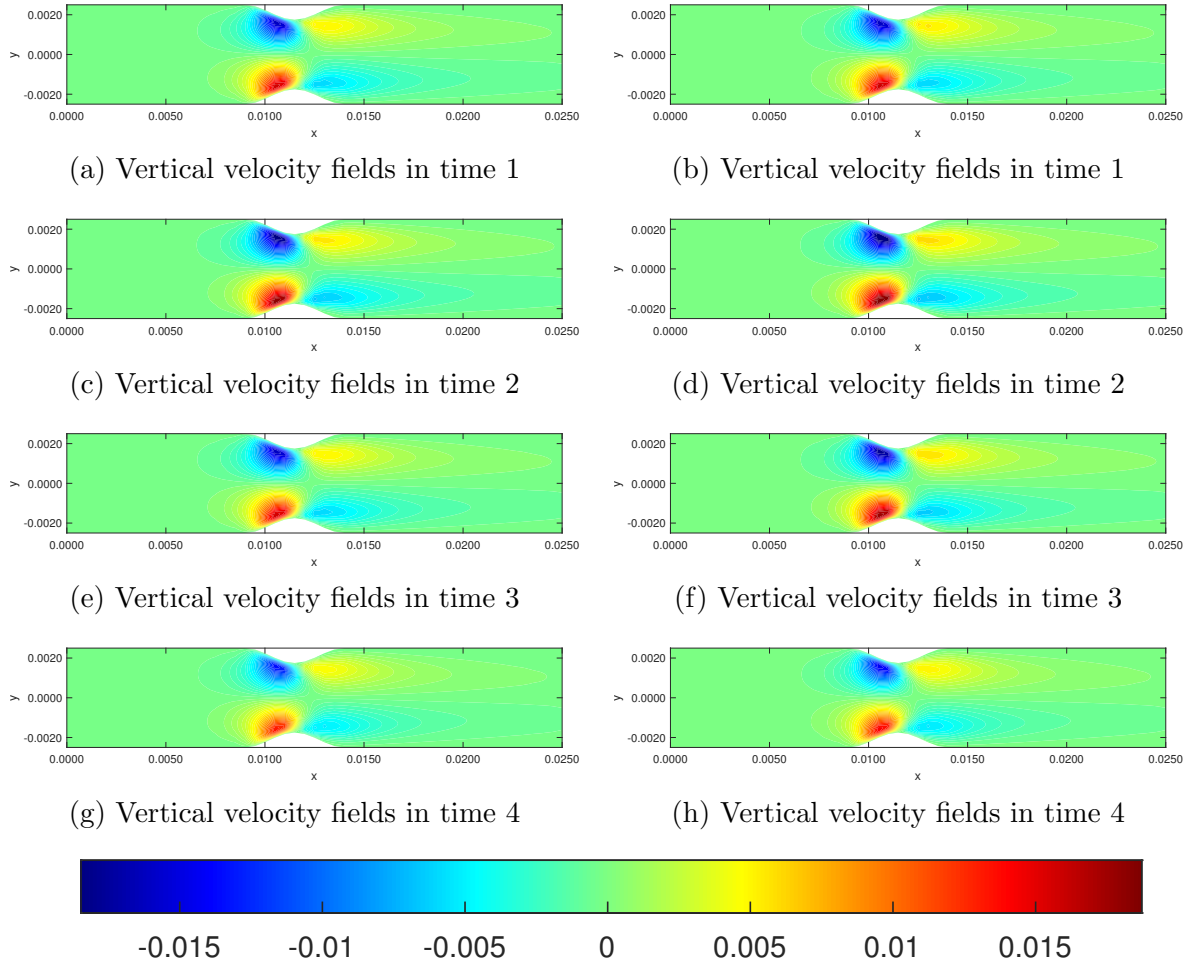


Figure 16: Vertical velocity v fields for different time instants of pressure sine in last period for stenosed channel for pressure correction method on left, for artificial compressibility method on right

deviations from the anticipated parabolic profile. Notably, the velocity within the constricted segment attains levels akin to those within an unobstructed channel, albeit marginally attenuated. This observation, as depicted in the comparison with Fig. 13, remains congruent with the outcomes obtained from the simulation involving steady inlet pressure. As anticipated, the maximal values of horizontal velocity occur during time 2, coinciding with the period of highest inlet pressure. The comparison between the two solvers reveals that the artificial compressibility method exhibits limitations in accurately responding to variations in pressure, resulting in a delayed adjustment of the velocity field, in contrast to the more responsive behavior demonstrated by the pressure correction method. Fig. 16 presents the spatial distribution of vertical velocity v across the channel. As expected, the vertical velocity remains nearly constant at the inlet and gradually becomes pronounced as the flow progresses towards the constriction. In this narrowed region, the fluid exhibits a distinct behavior, converging toward the axis of the channel. Subsequent to the apex of the constriction, the fluid diverges from the channel center, moving towards its periphery, albeit at a more subdued rate compared to its entrance into the constriction. Notably, the magnitude of the vertical velocity attains levels an order of magnitude lower compared to that of the horizontal velocity. Analogous to the horizontal velocity, the vertical velocity attains its maximum values

during the temporal instance denoted by time 2 in Fig. 14, coinciding with the phase of highest inlet pressure.

5.4.2 Conclusion

The primary objective of this section was to demonstrate the proficiency of the pressure corrections method solver in addressing intricate geometries. This capability was showcased through the utilization of a mesh simulating a stenosed vein, wherein we conducted an analysis of pressure and velocity fields at various temporal intervals within the oscillatory pressure regime. Remarkably, the attained outcomes exhibited notable parallels with the findings of simulations conducted under steady pressure conditions at the inlet.

It is important to note that while our investigation has yielded compelling insights, the absence of an analytical solution for this particular scenario underscores the need for further exploration. Specifically, a comprehensive study encompassing the influence of temporal and spatial discretization steps, as well as the initial simulation parameters, would greatly contribute to a more nuanced understanding of the system's behavior.

Comparison with artificial compressibility method shows the results are similar and given insight from comparison with analytical solution, we can expect the pressure corrections method yields results with higher degree of accuracy. It is important to note, however, that achieving this heightened accuracy entails an additional computational time investment.

5.5 Choosing optimal viscosity

The goal of this simulation is to determine an optimal viscosity value that can be used to approximate non-Newtonian fluids as Newtonian fluids. By employing this approximation, we aim to simplify the modeling process and reduce computational time, while still maintaining reasonable accuracy in the simulation results. Additionally, another objective of this research is to define a non-Newtonian equivalent of the Reynolds number, which can serve as a useful parameter for characterizing the flow regime in non-Newtonian fluid simulations. It is worth noting that previous studies [11]; [25]; [4]; [21]) have proposed various approaches in this field, but a consistent and experimentally validated definition of the Reynolds number for non-Newtonian fluids is still lacking. Thus, this research aims to contribute to the existing knowledge by exploring the optimal viscosity and establishing a meaningful non-Newtonian Reynolds number that can enhance the understanding and analysis of non-Newtonian fluid flow behavior.

5.5.1 Problem setting

The solver utilized in previous sections, employing the artificial compressibility method, will be used for the simulation on the three geometries described in 5.1. The simulations will be performed using various test viscosities, ranging from μ_0 to μ_{inf} . To assess the impact of non-Newtonian behavior, a power-law model will be employed, with the fluid properties set to resemble human blood. Specifically, the density ρ will be set to $1060 \text{ kg} \cdot \text{m}^{-3}$, the flow consistency index K will be set to $29.3 \cdot 10^{-3} \text{ Pa} \cdot \text{s}^\kappa$, and the flow behavior index κ will be set to 0.628.

To initialize the simulations, six different pressure differences will be imposed as initial conditions at the inlet. The initial pressure difference δp will be set to 5.1 Pa, which, for a Newtonian fluid with properties similar to blood, yields a velocity in the x -direction of 0.2, which is representative of flow velocities in larger human veins. The other pressure differences will be set as 0.5, 1.5, 2, 3, and 4 times δp .

For the curved channel geometry, the reference pressure difference will be set to $\delta p = 1$ Pa to ensure the stability of the numerical method employed.

To evaluate and compare the results between the Newtonian and non-Newtonian fluid simulations, the Euclidean norm ($\|\cdot\|_2$) of the difference in velocity fields will be calculated. The Euclidean norm is defined as follows:

$$\|\mathbf{v}_{\text{Newtonian}} - \mathbf{v}_{\text{non-Newtonian}}\|_2 = \frac{1}{N} \left(\sum_{i=1}^N \left(v_{\text{Newtonian}}^{(i)} - v_{\text{non-Newtonian}}^{(i)} \right)^2 \right)^{\frac{1}{2}}$$

where $\mathbf{v}_{\text{Newtonian}}$ and $\mathbf{v}_{\text{non-Newtonian}}$ represent the velocity fields of the Newtonian and non-Newtonian fluids, respectively, and $v_{\text{Newtonian}}^{(i)}$ and $v_{\text{non-Newtonian}}^{(i)}$ are the velocity components at each grid point or spatial location and N represents number of cells, to make the results of this norm independent on chosen grid.

By following this methodology, we aim to determine the optimal viscosity value that approximates the non-Newtonian behavior as Newtonian, facilitating the use of simplified models and saving computational time. Additionally, the evaluation of the velocity field differences using the Euclidean norm will provide insights into the impact of non-Newtonian characteristics on the flow behavior.

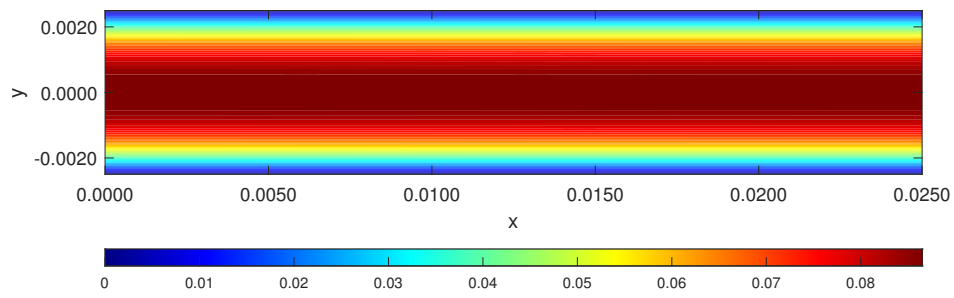
5.5.2 Simulation in straight channel

In the case of the straight channel, we can leverage certain assumptions to derive analytical solutions for the Navier-Stokes equations for both Newtonian and non-Newtonian fluids. These analytical solutions, as discussed in detail in Section 3.2.6 and Section 3.2.7, provide valuable insights into the flow behavior in the straight channel geometry. By obtaining analytical solutions, we can establish a baseline for comparison with the simulation results, thereby validating the accuracy and reliability of the simulation approach for different viscosities.

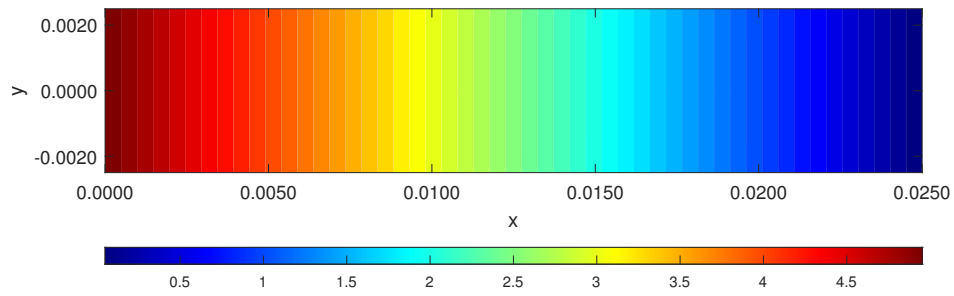
5.5.3 Results of simulations in straight channel

In Fig. 17, we present the velocity fields resulting from the simulation of non-Newtonian fluid in the straight channel, along with the corresponding viscosity field μ . These visualizations offer insights into the flow behavior and the distribution of viscosity within the channel.

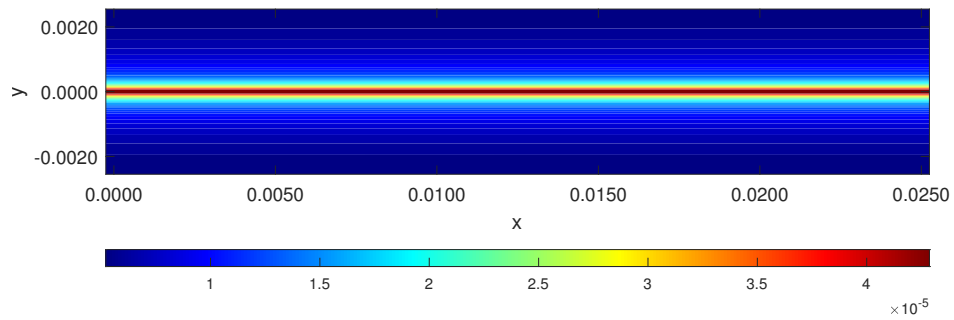
The velocity field illustrates the flow patterns within the straight channel. We observe the expected parabolic velocity profile, where the flow is faster near the center and slower near the walls. This velocity distribution is characteristic of laminar flow in a straight conduit. Additionally, the velocity field confirms the presence of flow in the x -direction, which is the primary direction of flow in the straight channel, and values of velocity in y -direction are reaching numerical zero.



(a) Horizontal velocity



(b) Pressure field



(c) Viscosity field

Figure 17: Results of simulation for Newtonian fluid on straight geometry for $\delta p = 5.1$ Pa

The viscosity field μ provides information about the distribution of viscosity within the channel. In this simulation, the viscosity remains relatively constant throughout the channel due to the absence of significant geometric variations or flow disturbances. This behavior is consistent with the Newtonian fluid assumption, where the viscosity is independent of the shear rate. However, in the center of the channel, viscosity suddenly peaks and reaches limiting viscosity μ_{lim} . Without this limitation, the theoretical viscosity would reach infinity.

The limitation of the viscosity field by the μ_{lim} value is crucial to maintain physically meaningful results. In non-Newtonian fluids, the viscosity can exhibit extremely high values at low shear rates or in regions of high deformation. However, by imposing the μ_{lim} constraint, we ensure that the viscosity values remain finite and realistic within the simulation. This approach allows us to accurately capture the flow behavior while avoiding unphysical or unrealistic viscosity values.

Fig. 18 illustrates the variations in velocity magnitudes for four selected viscosities that closely approximate the desired flow behavior of the non-Newtonian fluid in the straight channel. In these simulations, we observed a consistent pattern across all viscosities, with the most significant differences occurring in the center of the channel, where the velocity reaches its maximum. This observation aligns with our expectations based on the distinct velocity profiles exhibited by Newtonian and non-Newtonian fluids. For a detailed comparison of these velocity profiles, please refer to Fig. 19.

The observed pattern in the velocity magnitudes can be attributed to the differences in rheological properties between Newtonian and non-Newtonian fluids. Newtonian fluids exhibit a parabolic velocity profile, while non-Newtonian fluids, depending on their rheological behavior, may display altered velocity distributions.

5.5.4 Simulation in stenosed channel

The simulation was performed with the same set of initial conditions on a geometry, that has been gradually stenosed in the middle $\frac{1}{5}$ to 0.7 of its original diameter using *cosine* function as described in 5.1 simulating stenosis of vein. For this geometry, we expect the flow to accelerate in the constriction as well as appearance of velocity in y -direction.

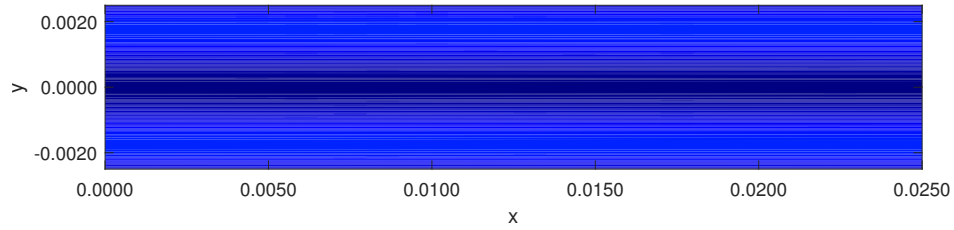
5.5.5 Results of simulations in stenosed channel

An example of reference overall velocity field of non-Newtonian fluid for $\delta p = 5.1$ Pa can be seen in Fig. 20.

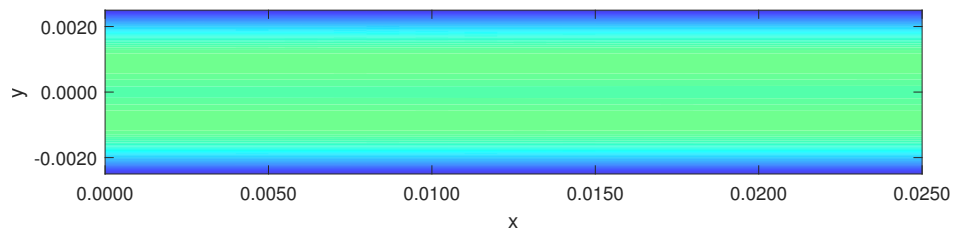
As expected, the flow exhibited a noticeable acceleration within the stenosed section of the channel. This acceleration can be attributed to the reduced cross-sectional area, resulting in higher flow velocities in comparison to the wider regions of the geometry.

In addition to the accelerated flow in the narrowing region, a non-negligible velocity component in the y -direction (transverse to the main flow direction) was observed. This phenomenon can be attributed to the asymmetric geometry of the stenosed channel, causing a pressure difference that induces fluid motion perpendicular to the primary flow direction.

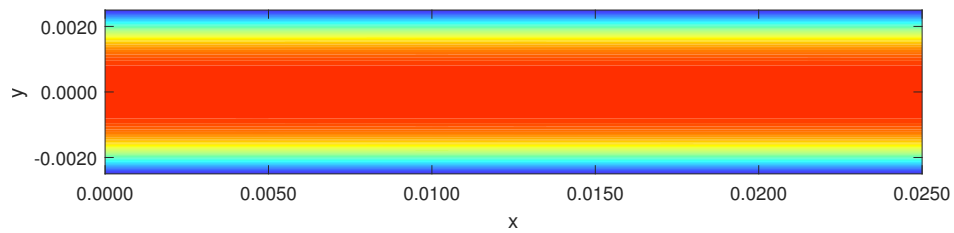
The simulation results indicated a significant pressure decay across the stenosed section of the channel. This pressure decay can be attributed to the increased fluid velocity and the restricted cross-sectional area.



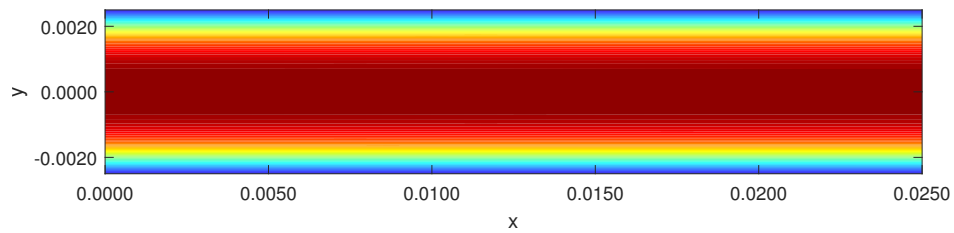
(a) $\mu = 0.006725 \text{ Pa} \cdot \text{s}$



(b) $\mu = 0.010000 \text{ Pa} \cdot \text{s}$



(c) $\mu = 0.016588 \text{ Pa} \cdot \text{s}$



(d) $\mu = 0.023156 \text{ Pa} \cdot \text{s}$

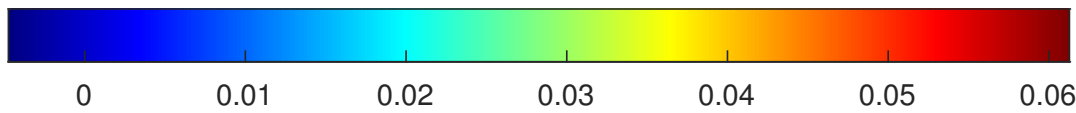


Figure 18: Difference in velocity magnitudes ($\mathbf{v}_{\text{Newtonian}} - \mathbf{v}_{\text{non-Newtonian}}$) for selected viscosities for $\delta p = 5.1 \text{ Pa}$ for straight channel

In the viscosity field within the stenosed part of the channel, we observe a characteristic shear-thinning behavior, which is typical for non-Newtonian fluids like blood. This phenomenon occurs as the shear rate increases, leading to a reduction in viscosity. This shear-thinning behavior is prominent within the stenosed section due to the higher flow velocities experienced in this region.

In the inlet and outlet the viscosity field closely resembles the viscosity field observed in the straight channel simulation shown in Fig. 17. The viscosity values in these regions are limited by the limiting viscosity (μ_{lim}), preventing the theoretical viscosity from reaching infinity.

Fig. 21 illustrates the variations in velocity magnitudes for four selected viscosities that closely approximate the desired flow behavior of the non-Newtonian fluid in the straight channel. In these simulations, we observed a consistent pattern across all viscosities, with the most significant differences occurring in the constriction of the channel, where the velocity reaches its maximum. For a detailed comparison of velocity profiles at the inlet and outlet of stenosed channel, please refer to Fig. 22. Upon closer examination, we observe that for a viscosity value of $\mu = 0.006725 Pa \cdot s$, the simulation of the Newtonian fluid closely replicates the profile of the non-Newtonian fluid near the edges of the channel. However, it is important to note that the maximum velocity difference between the two simulations is higher in this case.

In Fig. 23, we present the Euclidean norm of the difference between the velocity magnitudes of the Newtonian and non-Newtonian fluids for various pressure differences. This norm provides an overall measure of the discrepancy between the two simulations.

Upon examination, we observe that as the pressure difference increases, the velocities and shear rates in the channel also increase. Consequently, to accurately simulate this behavior, the optimal viscosity for the Newtonian approximation should be closer to the limiting viscosity μ_{∞} . This choice accounts for the higher velocities and shear

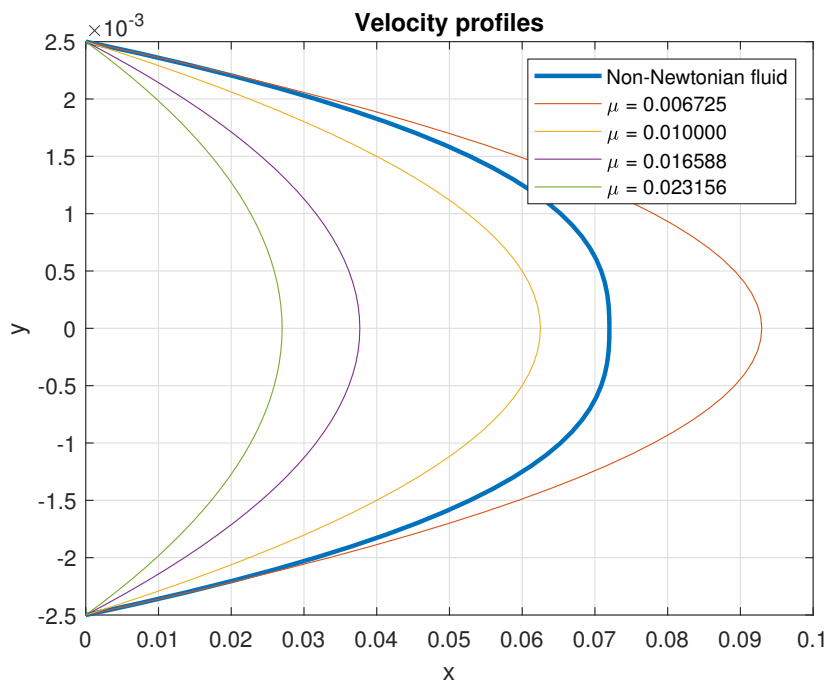
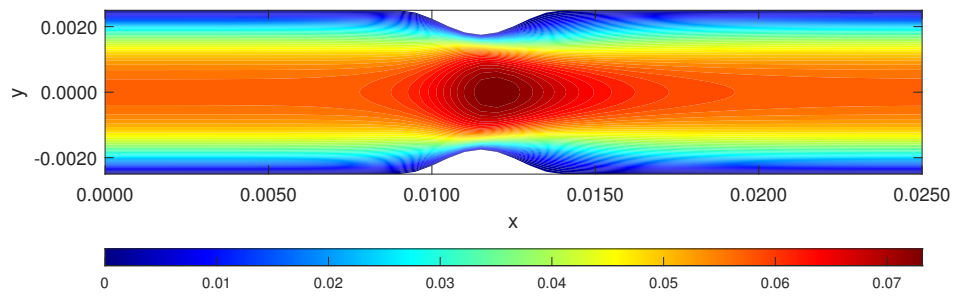
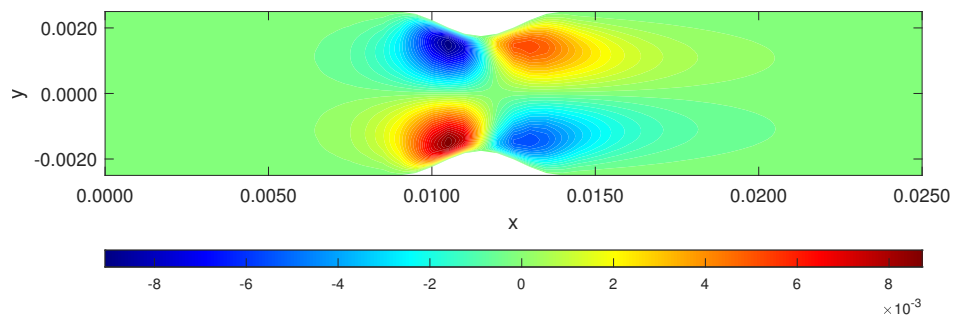


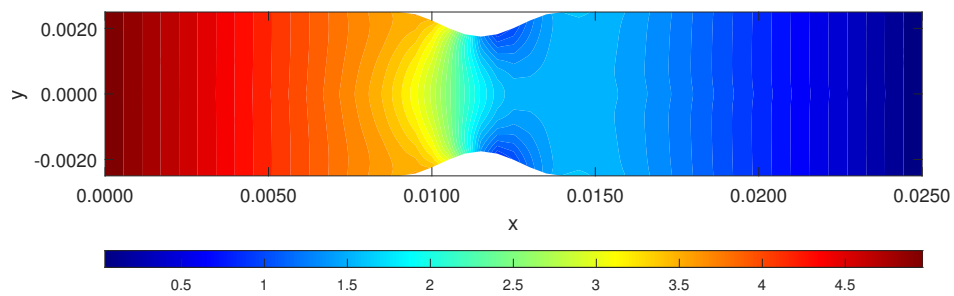
Figure 19: Velocity profiles for selected viscosities for $\delta p = 5.1 Pa$



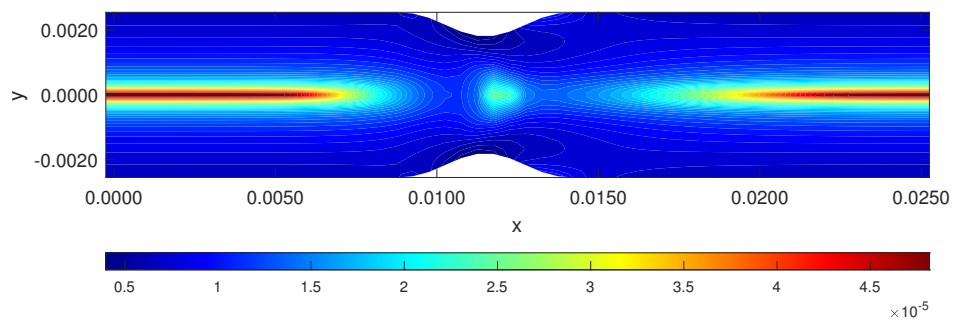
(a) Horizontal velocity u



(b) Vertical velocity v

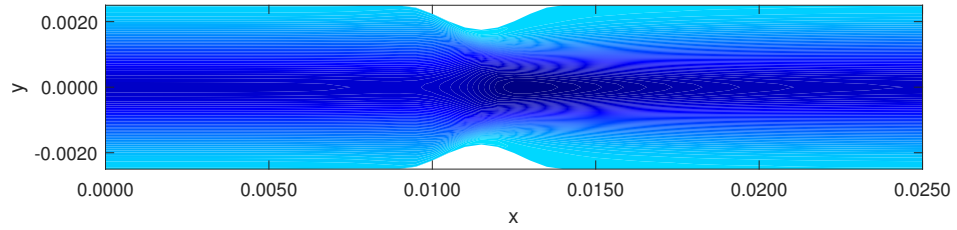


(c) Pressure field

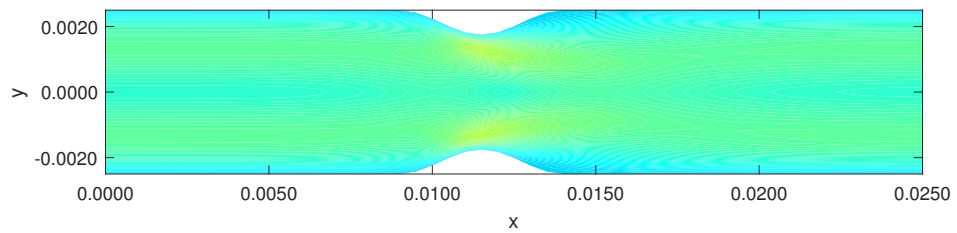


(d) Viscosity field

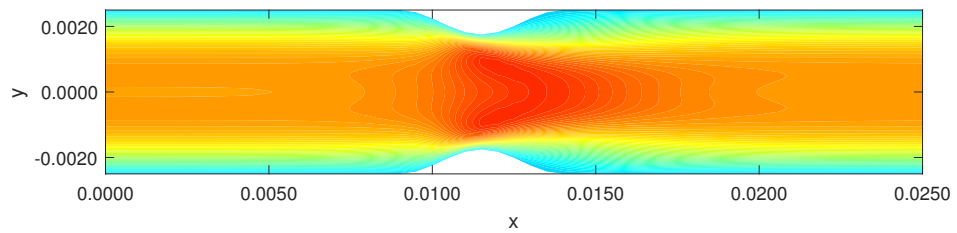
Figure 20: Results of simulation for Newtonian fluid on stenosed geometry for $\delta p = 5.1$ Pa



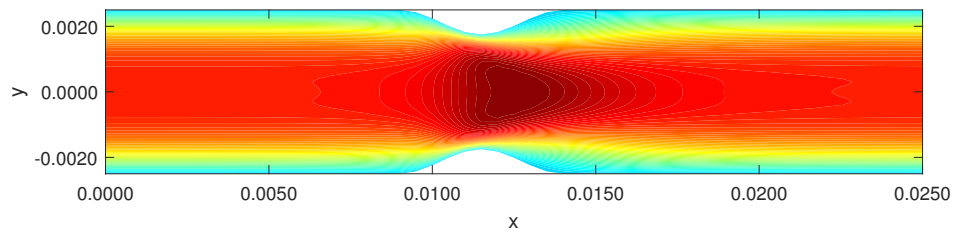
(a) $\mu = 0.006725 \text{ Pa} \cdot \text{s}$



(b) $\mu = 0.010000 \text{ Pa} \cdot \text{s}$



(c) $\mu = 0.016588 \text{ Pa} \cdot \text{s}$



(d) $\mu = 0.023156 \text{ Pa} \cdot \text{s}$

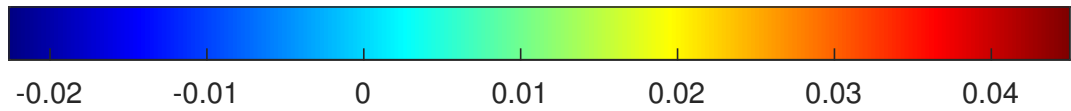


Figure 21: Difference in velocity magnitudes ($\mathbf{v}_{\text{Newtonian}} - \mathbf{v}_{\text{non-Newtonian}}$) for selected viscosities for $\delta p = 5.1 \text{ Pa}$ for stenosed channel

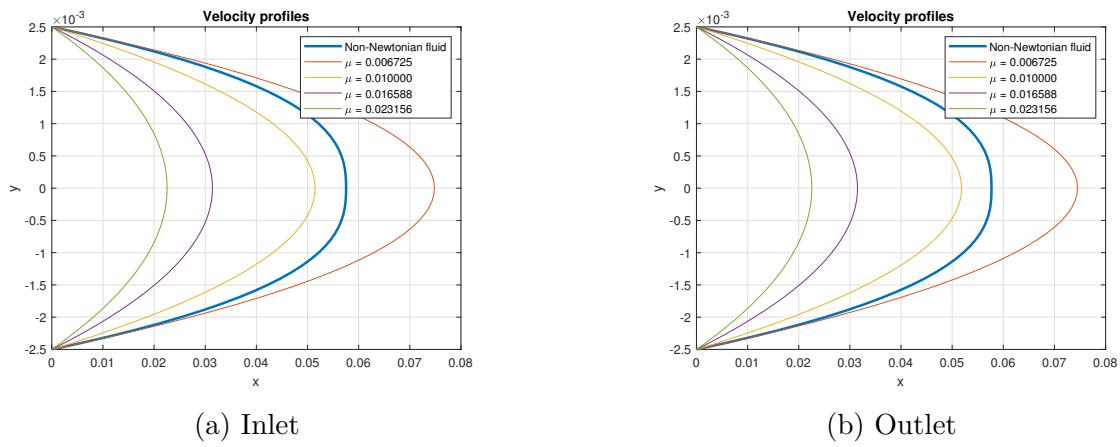


Figure 22: Velocity profiles of stenosed channel for selected viscosities for $\delta p = 5.1$ Pa

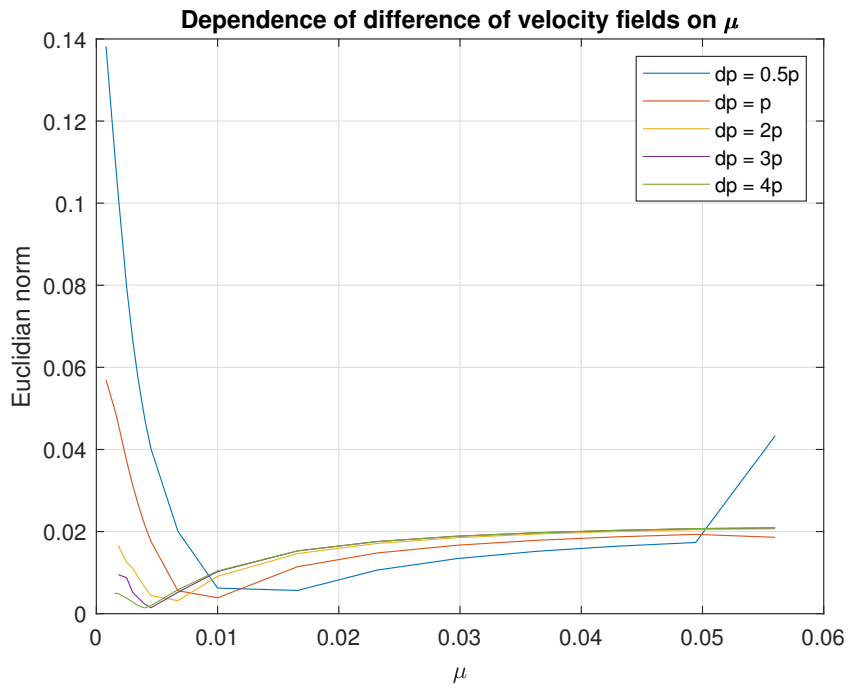


Figure 23: Euclidian norms of difference of velocity magnitudes for stenosed channel

rates associated with larger pressure differences.

Conversely, as the pressure differences decrease, the optimal Newtonian viscosity moves closer to the viscosity at low shear rates μ_0 . This adjustment considers the lower velocities and shear rates associated with smaller pressure differences.

It is important to note that as we deviate further from the optimal viscosity values, specifically towards μ_∞ , the error in our simulation results increases more rapidly compared to using viscosities closer to μ_0 .

Described behavior of the optimal viscosity and the associated error trends align with the characteristics typically observed in shear-thinning fluids.

5.5.6 Simulation in curved channel

To simulate the flow in the curved channel, we will employ the same solver used in the previous sections, utilizing the artificial compressibility method. The simulated geometry should resemble real-world scenario, such as blood vessels with bends or arteries with curvatures.

The mesh is generated in MATLAB and is set to have same length as the straight and stenosed channel, but is bent by $\frac{\pi}{2}$ radians (90°).

To maintain stability during the simulation, the reference pressure difference δp will be set to 1 Pa. This choice ensures accurate and reliable simulation results in reasonable computational time without compromising stability.

The simulation will be performed for various test viscosities, ranging from μ_0 to μ_∞ , while employing the power-law model to represent the non-Newtonian behavior of the fluid. To mimic human blood properties, the fluid properties will be set to a density $\rho = 1060 \text{ kg} \cdot \text{m}^{-3}$, a flow consistency index $K = 29.3 \cdot 10^{-3} \text{ Pa} \cdot \text{s}^\kappa$, and a flow behavior index $\kappa = 0.628 \text{ Pa} \cdot \text{s}$ for simulation of non-Newtonian fluid.

5.5.7 Results on simulations in curved channel

In Fig. 24, we present the results obtained from the simulation of non-Newtonian fluid in the curved channel, along with the corresponding viscosity field μ .

As anticipated, the flow within the channel exhibits an increase in velocity towards the center, while maintaining zero velocity at the edge of the computational domain to fulfill the boundary conditions. This behavior is consistent with the observations made in the straight canal simulation. However, it is worth noting that the velocity field is not entirely symmetric, with the peak velocity occurring closer to the inner wall of the curvature. This asymmetry is an interesting characteristic that distinguishes the flow behavior within the curved channel from that in a straight canal.

Analyzing the viscosity field μ , we observe minimal variations along the curvature of the canal. The viscosity reaches its maximum near the center of the channel, closer to the inner wall of the curved channel, where it reaches the maximum viscosity value μ_{\max} . This viscosity asymmetry follows the velocity field and is a typical behavior observed in non-Newtonian fluids, such as blood.

The pressure field exhibits a regular, almost linear distribution along the length of the channel. This observation indicates a gradual pressure decay as the fluid flows through the curved channel, conforming to the expected behavior in such geometries.

Fig. 25 illustrates the variations in velocity fields for four selected viscosities that closely approximate the desired flow behavior of the non-Newtonian fluid in the curved channel. In these simulations, we observed a consistent pattern across all viscosities,

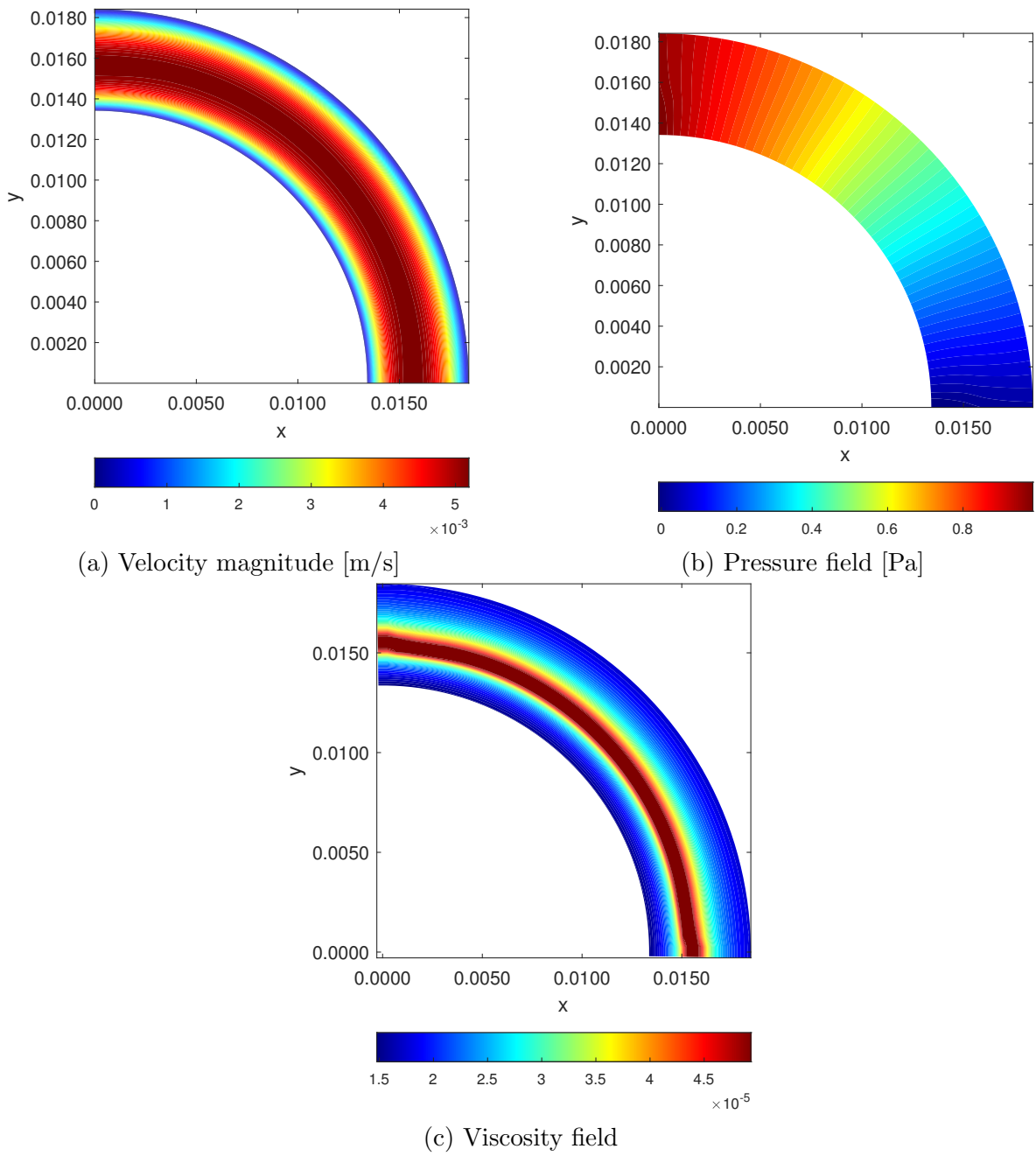


Figure 24: Results of simulation for Newtonian fluid in curved channel for $\delta p = 1$ Pa

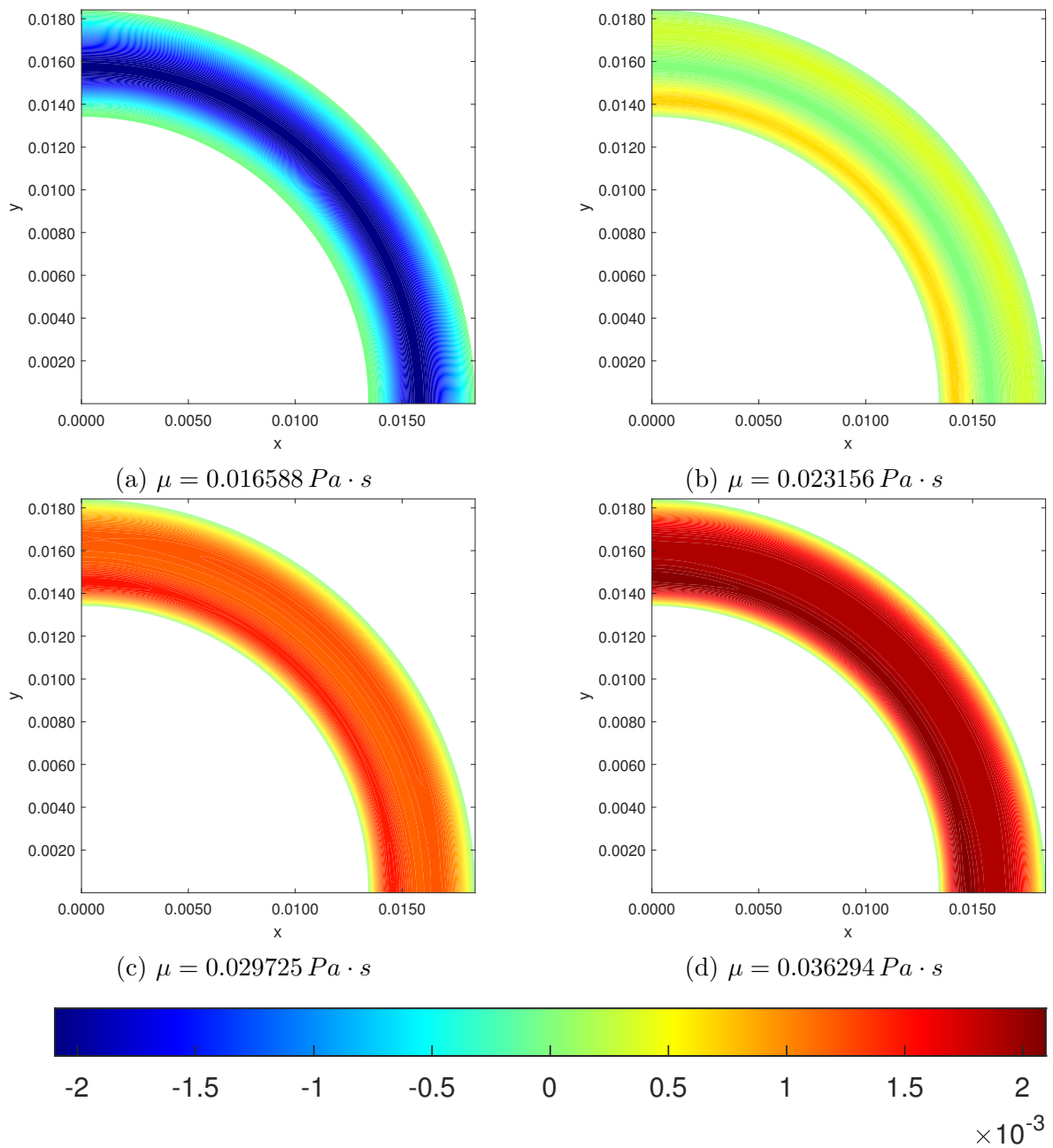


Figure 25: Difference in velocity magnitudes ($\mathbf{v}_{\text{Newtonian}} - \mathbf{v}_{\text{non-Newtonian}}$) for selected viscosities for $\delta p = 1.0 \text{ Pa}$ for curved channel

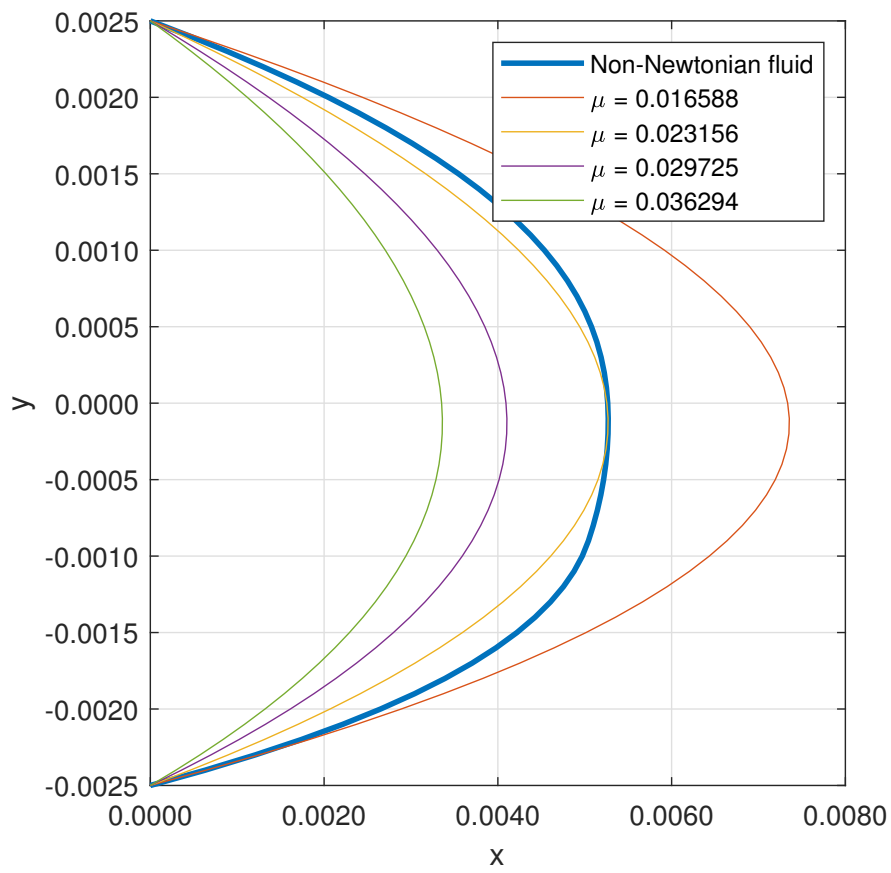


Figure 26: Velocity profiles at outlet for selected viscosities for $\delta p = 1.0$ Pa for curved channel

with the most significant differences occurring where the velocity reaches its maximum. For a detailed comparison of velocity profiles, please refer to Fig. 26. Upon closer examination, we observe that for a viscosity value of $\mu = 0.023156 Pa \cdot s$, the simulation of the Newtonian fluid closely replicates the profile of the non-Newtonian fluid reaching same maximal velocity. Furthermore, in this figure, we can observe the offset of the peak velocity towards the inner wall of curvature. In Fig. 27, we present the Euclidean norm of the difference between the velocity fields of the Newtonian and non-Newtonian fluids for various pressure differences, with exclusion of certain peak values approaching μ_∞ . This norm provides a comprehensive measure of the discrepancy between the two simulations and serves as a quantitative assessment of the simulation accuracy.

Upon examination of the norm values, we observe a clear relationship between the pressure differences and the resulting velocities and shear rates within the channel. As the pressure difference increases, the velocities and shear rates also increase accordingly. Consequently, to accurately capture this behavior, the optimal viscosity for the Newtonian approximation should be closer to the asymptotic viscosity μ_∞ . This choice takes into account the higher velocities and shear rates associated with larger pressure differences, ensuring a more faithful representation of the flow dynamics.

Conversely, as the pressure differences decrease, the optimal Newtonian viscosity moves closer to the viscosity at low shear rates μ_0 . This adjustment is necessary to account for the lower velocities and shear rates observed with smaller pressure differences, maintaining accuracy in simulating the flow behavior.

Importantly, it should be noted that as we deviate further from the optimal viscosity values, particularly towards μ_∞ , the error in our simulation results increases more rapidly compared to using viscosities closer to μ_0 . This highlights the sensitivity of the simulation accuracy to the choice of viscosity approximation, emphasizing the importance of selecting viscosities within an appropriate range to achieve reliable results.

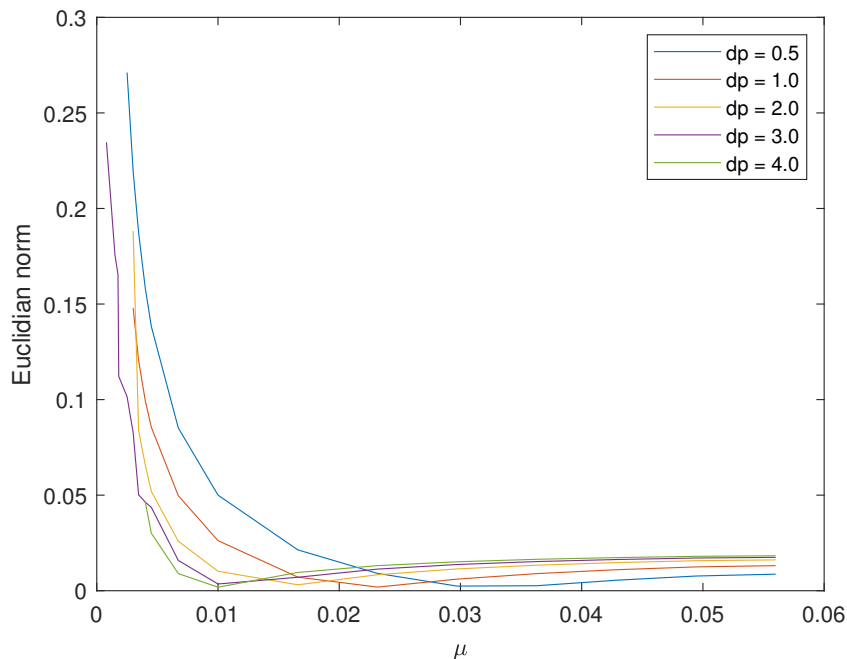


Figure 27: Euclidian norms of difference of velocity magnitudes for curved channel

The observed behavior of the optimal viscosity and the associated error trends align with the characteristics typically observed in shear-thinning fluids. Furthermore, these findings are consistent with the trends identified in previous simulations, which also demonstrated similar values of the Euclidean norm approaching μ_0 .

5.5.8 Conclusion

By considering the relationship between pressure differences, velocity fields, and the optimal viscosity, we gain valuable insights into the behavior of non-Newtonian fluids. These insights contribute to the development of accurate simulation methodologies for shear-thinning fluids, enabling more reliable predictions of flow behavior and enhancing our understanding of fluid dynamics in complex geometries.

The simulation results align with the characteristics of shear-thinning fluids expected from simulations of blood. The choice of optimal viscosity depends on the specific properties of the simulation. In cases where higher maximal velocities are observed, the optimal viscosity tends to be closer to the asymptotic viscosity μ_∞ . Conversely, as the velocity decreases, the optimal viscosity tends to move towards the viscosity at low shear rates μ_0 .

However, it is generally more favorable to choose a viscosity approximation closer to μ_0 as the difference in velocities between the Newtonian and non-Newtonian simulations is lower. This choice minimizes the error in the simulation results and provides a closer approximation to the behavior of the non-Newtonian fluid.

It is important to note that the evaluation of the results was based on the difference in velocity fields, which can be related to the difference in flow rate. However, it is crucial to consider that the choice of the optimal viscosity can vary depending on the desired criteria. Different criteria, such as pressure drop, flow rate, wall shear stress, or other flow characteristics, may lead to different optimal viscosity selections.

By acknowledging the influence of simulation properties and the trade-off between accuracy and computational efficiency, we can make informed decisions regarding the optimal viscosity approximation for the simulation of shear-thinning fluids. These considerations enhance our understanding of the flow behavior and contribute to the development of reliable simulation methodologies for non-Newtonian fluids.

6 Conclusion

The primary objective of this work was to present numerical simulations of incompressible Newtonian fluids, with a specific focus on their application in the field of biomedicine. These results were presented in section Numerical experiments. However, the background for these simulations was laid in previous sections. For clearer presentation of aims of this work, we will provide conclusion for each section.

Physical model Section Physical mode fulfills first objective of this work. We presented generalized Newtonian fluids and key properties of blood and described power-law model fluid, that was later used to describe non-Newtonian behavior of blood during simulations.

Mathematical model At the beginning of this section, we introduced Reynolds number and Womersley number, dimensionless number used to describe flow characteristics. We then derived basic equations of fluid dynamics, mainly continuity equation and Navier-Stokes equations. We presented analytical solution of these equations for three dimensional flow in tube in radial coordinates and for two dimensional flow in cartesian coordinates for three simplified cases of Newtonian fluid driven by constant pressure, power-law model fluid driven by constant pressure and Newtonian fluid driven by oscillating pressure. This answers second task of this work.

Numerical model In this section, we have outlined the process of discretizing the Navier-Stokes equations in a two-dimensional case using finite volumes method. We presented coupling of pressure and velocity using artificial compressibility method and derived pressure equation for pressure correction method with equations using finite volumes method to express poisson equation.

Numerical experiments We implemented obtained equations into own numerical code in MATLAB and performed various simulations of fluid with blood-like properties with different aims. First set of simulations aimed to show results for non-stationary flow and to compare artificial compressibility method and pressure correction method. First simulation case on straight channel was used to compare results with analytical solution derived earlier in this work, as well as compare the two used methods. in second test case, flow through stenosed channel, we showed ability to simulate more complex geometry and we presented results for both methods. For second set of simulations, we used solver using artificial compressibility method and we presented difference between flow of non-Newtonian and Newtonian fluid. Power-law model with constants set to fit behavior of blood was used and we performed simulations for three different two dimensional geometries with six pressures set on the inlet and various viscosities for Newtonian fluid. We discussed optimal choice of viscosity to use in simulations of Newtonian fluid in order to simulate non-Newtonian fluid, when aim of the simulation is similar velocity profile. More detailed conclusion follows each test case in section Numerical experiments. These simulations answer the rest of tasks for this work.

This work could be further developed by expanding for three dimensional cases, implementation of power-law model in solver using pressure correction method, rewriting the solver in different language and improving its performance, implementing of

two-step method into pressure correction method, improving performance of artificial compressibility method in simulations with oscillating pressure by using dual time stepping method.

References

- [1] H. A. Barnes. Thixotropy - a review. *Journal of Non-Newtonian Fluid Mechanics*, 70(1):1–33, 1997.
- [2] R. B. Bird, R. C. Armstrong, and O. Hassager. *Dynamics of Polymeric Liquids, Volume 1: Fluid Mechanics*. Wiley-Interscience, 2nd edition, 1987.
- [3] S. Chien, S. Usami, H. M. Taylor, and J. Lundberg. Rheology of blood. *Annual review of fluid mechanics*, 19(1):61–86, 1987.
- [4] R. A. Chilton and R. Stainsby. Pressure loss equations for laminar and turbulent non-newtonian pipe flow. *Journal of Hydraulic Engineering*, 124:522–529, 1998.
- [5] Y. Cho and K. Kensey. Effects of the non-newtonian viscosity of blood on flows in a diseased arterial vessel. part 1: Steady flows. *Biorheology*, 28:241–62, 02 1991.
- [6] A. J. Chorin and J. E. Marsden. *Mathematical and Computational Methods for Compressible Flow*. Springer, 1993.
- [7] M. O. Deville. *An Introduction to the Mechanics of Incompressible Fluids*. Springer, 2021.
- [8] M. Feistauer. *Mathematical and Computational Methods for Compressible Flow*. Oxford University Press, 1993.
- [9] M. Feistauer. *Numerical Solution of Time-Dependent Advection-Diffusion-Reaction Equations*. Springer, 2003.
- [10] M. Feistauer, J. Felcman, and I. Straškraba. *Mathematical and Computational Methods for Compressible Flow*. Oxford Science Publications, 2003.
- [11] R. W. Hanks. Low reynolds number turbulent pipeline flow of pseudo homogeneous slurries. In *Proc. Hydrotransport 5 Conf.*, Hanover, GFR, 1978.
- [12] A. Lancmanová. Porovnání numerických metod pro nestacionární simulace nestlačitelného proudění, 2020.
- [13] L. D. Landau and E. M. Lifshitz. *Fluid Mechanics*. Theoretical Physics, Volume 6. Institute of Physical Problems, USSR Academy of Sciences, Moscow, second edition revised edition, 1959.
- [14] R. G. Larson. *The Structure and Rheology of Complex Fluids*. Oxford University Press, 1999.
- [15] C. Loudon and A. Tordesillas. The use of the dimensionless womersley number to characterize the unsteady nature of internal flow. *Journal of theoretical biology*, 191:63–78, 1998.
- [16] J. Mazumdar. *An Introduction to Mathematical Physiology and Biology*. Cambridge Studies in Mathematical Biology. Cambridge University Press, 1999.

- [17] N. McBride. Density and viscosity of liquid water and ice-calculation method for the international temperature scale of 1990. *Journal of Physical and Chemical Reference Data*, 34(1):91–195, 2005.
- [18] M. D. Pedley and M. Rogerson. *Flow and transport in porous media and fractured rock: from classical methods to modern approaches*. Cambridge University Press, 2016.
- [19] D. R. Peterson and J. D. Bronzino. *Biomechanics: Principles and Applications*. CRC Press LLC, Washington, second edition edition, 2003.
- [20] L. Pirkel. Numerical simulations of incompressible flows with variable viscosity, 2007.
- [21] M. Rudman and H. M. Blackburn. Turbulent pipe flow of non-newtonian fluids. In *Computational Fluid Dynamics 2002*, Berlin, Heidelberg, 2003. Springer Berlin Heidelberg.
- [22] O. San and A. E. Staples. An improved model for reduced-order physiological fluid flows. *Journal of Mechanics in Medicine and Biology*, 12(3):125–152, 2012. arXiv:1212.0188.
- [23] H. Schlichting and K. Gersten. *Boundary-Layer Theory*. Springer, 8th edition, 2000.
- [24] R. Skalak and S. Chien. *Biomechanics: Mechanical Properties of Living Tissues*. Springer Science & Business Media, 1988.
- [25] P. T. Slatter. Transitional and turbulent flow of non-newtonian slurries in pipes. 1995.
- [26] I. Sládek, K. Kozel, and Z. Jaňour. On the 2d-validation study of the atmospheric boundary layer flow model including pollution dispersion. pages 323 – 333, 11 2009.
- [27] R. Wells and W. Slaughter. Thixotropic behavior of blood. *Biorheology*, 44(4):243–256, 2007.
- [28] F. M. White. *Viscous Fluid Flow*. McGraw-Hill Education, 3rd edition, 2006.
- [29] Wikipedia contributors. Non-newtonian fluid — Wikipedia, the free encyclopedia, 2023. [Online; accessed 12-August-2023].
- [30] J. R. Womersley. Method for the calculation of velocity, rate of flow and viscous drag in arteries when the pressure gradient is known. *Journal of Physiology*, 127(3):553–563, 1955.